# NUMERICAL SIMULATIONS OF THE INTERNAL TIDE IN A SUBMARINE CANYON

by

Emil T. Petruncio[1], Jeffrey D. Paduan, and Leslie K. Rosenfeld

Department of Oceanography
Naval Postgraduate School
Monterey, CA 93943

[1] Now at Naval Meteorology and Oceanography Command Headquarters (COMNAVMETOCCOM), Stennis Space Center, MS 39529

Submitted to *Ocean Modelling*

November 22, 2000

Corresponding author address: Dr. Jeffrey Paduan, Code OC/Pd, Naval Postgraduate School, 833 Dyer Rd., Rm. 328, Monterey, CA 93943.
E-mail: paduan@oc.nps.navy.mil

## ABSTRACT

Three-dimensional numerical simulations of the generation and propagation of the semidiurnal internal tide in a submarine canyon with dimensions similar to those of the Monterey Canyon are carried out using a primitive equation model. Forcing with just sea level at the offshore boundary in an initially horizontally homogeneous ocean with realistic vertical stratification, internal tides are generated at the canyon foot and rim, and along portions of the canyon floor. The results compare favorably with observations, both indicating enhancement of energy along the canyon floor propagating at an angle consistent with linear internal wave theory. Due to the earth's rotation, internal tide energy is distributed asymmetrically in the cross-canyon direction, favoring the southern side. The effect of canyon floor slope is explored, with the finding that small changes in the slope result in large changes in the amount and distribution of the internal tide energy. Canyons whose floors are subcritical with respect to the semidiurnal frequency along their entire length have very little baroclinic energy, whereas canyons that are near critical along much of their length, such as the Monterey Canyon, develop strong internal tides that propagate shoreward. Canyons that are near-critical at their mouths but supercritical further inshore generate the most internal tidal energy overall, although little of it makes it onto the continental shelf shoreward of the canyon head. The effects of internal tides within the canyons can be seen outside the canyons as well. Water is transported from depth onto the adjacent continental shelf along the canyon rims. This tidal pumping can be responsible for along-shore internal tide propagation and tidal-period surface currents with relatively small horizontal scales of variability.

## 1. Introduction

The presence of internal waves at tidal frequencies (internal tides) greatly complicates the problem of forecasting coastal tidal currents. In addition, the turbulent mixing due to the internal wave field associated with abrupt topography has recently been shown to be of potential significance in determining the abyssal circulation on basin-wide scales (Polzin et al. 1997; Munk and Wunsch 1998). These facts point to the need to understand the interaction between open ocean tidal forcing and the three-dimensional topographic features of the continental margins. Among these topographic features are submarine canyons, and it has long been speculated that submarine canyons can act as traps for internal waves in certain frequency bands (Gordon and Marshall 1976) thus greatly amplifying their energy (Hotchkiss and Wunsch 1982). There have been numerous analytical studies of the generation (e.g. Baines 1974; Sandstrom 1976) and propagation (e.g. Wunsch 1968; Wunsch 1969) of internal waves on sloping bottoms. Recently, two-dimensional numerical studies (Holloway 1996; Xing and Davies 1996) and a three-dimensional numerical study (Cummins and Oey 1997) have been accomplished. While several field experiments report on the internal wave field in canyons (see Petruncio et al. 1998, hereafter PRP98, for a review), modeling results are limited to a set of wave tank experiments (Baines 1983). This study extends the state-of-the-art by applying a primitive equation model to the study of internal tide generation and propagation in the presence of a canyon, and by comparing the model results with observations.

Observations of the internal tide in Monterey Canyon by PRP98 motivated this numerical study. They reported baroclinic tidal currents an order of magnitude stronger than the estimated barotropic currents, with potential and kinetic energy concentrated along characteristic ray paths calculated from linear theory according to:

$$c = \tan\theta = (\omega^2 - f^2)^{\frac{1}{2}}(N^2 - \omega^2)^{-\frac{1}{2}}, \qquad (1)$$

where $\theta$ is the angle the group velocity vector makes with the horizontal, and $\omega$, $N$, and $f$ are the wave, buoyancy and inertial frequencies, respectively. The high resolution field observations

obtained in Monterey Bay present a unique opportunity to compare observed and numerically modeled internal tide propagation in a canyon.

The goal of this process study is to gain insight into how canyon geometry affects the generation, propagation, and dissipation of internal tides. We applied the primitive equation Princeton Ocean Model (POM) (Blumberg and Mellor 1987) to a domain with tidal forcing and density stratification akin to that found in Monterey Canyon. The idealized canyon used in the control experiments approximates the size and shape of Monterey Canyon. It includes a sloping floor, sloping sides, and narrows toward the head, a combination of elements difficult to replicate in a laboratory model, together with stratification, rotation, and tidal forcing. Perénne et al. (1997) studied a similar configuration using both model and laboratory approaches for the barotropic case and showed the ability of canyon topography to rectify oscillatory flows.

POM was originally designed to address mesoscale phenomena with time scales ranging from tidal to monthly, depending on domain size and grid resolution (Blumberg and Mellor 1987, Mellor 1996). It includes a free surface, sub-grid scale mixing parameterizations, and a $\sigma$ -(sigma) coordinate system in the vertical dimension, all of which are likely to be important for studying the internal tides in a submarine canyon. The $\sigma$ -coordinate transformation scales the z-level according to the water depth, such that at the free surface $\sigma = 0$ ($z = 0$), and at the bottom $\sigma = -1$ ($z = -H$). This results in terrain-following vertical levels and allows high resolution of surface and bottom boundary layers over variable bathymetry.

Huthnance (1989) notes the importance of appropriately representing the buoyancy frequency profile and the internal wave characteristic in numerical simulations of internal tides, and points out that these can be described better by levels or spectra in $z$ than by layers. Additionally, he points out that vertically stretched coordinates offer the advantage of "more easily describing $\nabla H$" (i.e., bottom slope, $\gamma$), which is important due to the sensitivity of internal wave reflections to the ratio $\gamma / c$. Furthermore, Kowalik and Murty (1993) state: "The resolution of the vertical processes by a constant layer thickness often fails to reproduce the processes in the region of abrupt topography variations or in the surface or bottom boundary layers." $\sigma$-coordinate models do,

however, have their own limitations in the presence of steep topography as pointed out by Haney (1991) and Kowalik and Murty. This error source is minimized by the use of high vertical and horizontal grid resolution, and by subtraction of a reference state density field before pressure gradient calculations are conducted (Mellor et al. 1994).

The modeling studies confirm that canyons can act to amplify internal tides relative to those propagating over the adjacent continental slope and shelf. Several features of the internal tide in Monterey Canyon are reproduced in the idealized simulations, including shoreward propagation of internal tide energy along characteristic ray paths, bottom-intensified current and density oscillations, and "tidal pumping" of cooler water onto the shelf near the canyon head. A feature of the internal tide which was suggested by the cross-canyon measurements in Monterey Canyon, and confirmed by this modeling study, is the concentration of energy along the southern canyon wall due to rotational effects.

The remainder of this paper is outlined as follows. In Section 2, previous applications of POM to the study of barotropic and baroclinic tides are briefly outlined, while in Section 3 details of the model setup for this study, including forcing functions and boundary conditions, are provided. Results from simulations using several different canyon floor slopes are presented in Section 4 with focus on the case most similar in shape to Monterey Canyon. Section 5 provides a discussion of trapped wave theory and how it may apply to internal tides in a canyon, along with further comparisons to observations from Monterey Canyon. Finally, conclusions about this study and the general applicability of primitive equation modeling to the study of internal tides are presented in Section 6.

## 2. Previous tidal applications of POM

Numerous applications of POM to simulate barotropic tides (Blumberg and Kantha 1985, Galperin and Mellor 1990, O'Connor 1991, Lewis et al. 1993) have reproduced observed coastal sea

level variations with reasonable accuracy, but the current fields associated with barotropic simulations can be expected to match observed currents only in shallow, well mixed seas and estuaries. Oey et al. (1985), Foreman (1995), and Xing and Davies (1996) note the importance of accounting for stratification in numerical simulations of tidal currents. However, even when density stratification is properly represented, numerical simulations may fail to accurately represent observed tidal currents unless bathymetric variations are sufficiently resolved as well.

In a study of baroclinic circulation in the northeast Atlantic shelves and seas (Oey and Chen 1992; Oey et al. 1992), tidal forcing was employed primarily to contribute to realistic bottom friction for the study of subtidal currents. While mean currents were accurately reproduced, the model tidal current fields were generally weaker than observed, and Oey et al. (1992) attribute this discrepancy to insufficient vertical resolution and smoothing of bathymetric regions with significant variation, such as trenches and ridges.

Most significant to this study is the work of Holloway (1996) who used POM specifically to simulate the internal tides over cross sections of the Australian North West Shelf. Holloway's simulations used the M2 sea level constituent for forcing and incorporated real topography in the cross-shore direction. Holloway's simulations reproduced a number of features of the internal tide that are consistent with his field measurements, including onshore propagation from the shelf break of a predominantly first mode wave, and little energy reaching the inner portion of a 150-200 km wide shelf. Bottom-intensified currents near critically-sloping bathymetry were in qualitative agreement with observations, but the amplitude of the isopycnal oscillations near the generation site were much weaker than observed (2 m vs. 10 m). He attributes some of the disparity between the modeled and observed internal tides to his 2-D simplification of the actual bathymetry, in which alongshore bathymetric variation was ignored.

Recently, a remarkable study by Cummins and Oey (1997), using a three-dimensional, tidally forced POM simulation of the continental shelf off northern British Columbia, mapped both barotropic and baroclinic tidal currents in the presence of realistic bathymetry. The internal tide in their study, whose distribution was sensitive to the locations of the major topographic features,

significantly enhanced the overall dissipation rates computed for the barotropic tide, both through wave radiation and through increased bottom friction. Most of the internal tide energy in their study propagates offshore from the shelf break, although evidence is presented for onshore propagation associated with several complex topographic features. The offshore baroclinic energy flux, integrated along the 800 km of their model domain, is five times larger than the two-dimensional, analytical estimates of Baines (1982), prompting Cummins and Oey to conclude that "...incorporation of stratification effects in three-dimensional models may be necessary to simulate in a realistic fashion the dissipation of semidiurnal constituents over continental shelves." Our present study differs from that of Cummins and Oey (1997) in that we focus on even smaller scales and the sensitivity of internal tide production to the particular shape of topographic features along the continental margin, particularly submarine canyons.

## 3. The numerical model

### *a. Set up of the model domain*

The bathymetry used for these simulations is idealized in order to facilitate a study of the effects of various floor slopes on internal tides, but the basic features are representative of the relatively steep continental slope and narrow shelf typical of the central California coast. The relative simplicity of the model bathymetry, as compared to the actual Monterey Bay bathymetry (Figure 1), permits easier identification of internal tide generation sites and propagation paths. Additionally, the performance of boundary conditions in transmitting baroclinic energy out of the domain can be monitored more precisely than would be the case if multiple internal wave generation sites were present. Additional model runs with more realistic bathymetry are in progress, but they are beyond the scope of this initial study.

The domain includes a 2500 m deep basin, a continental slope with a maximum gradient of 7.15°, and a 20 km wide shelf, 100 m in depth (Figure 1). The shelf and slope are incised by a single canyon perpendicular to the coast. The width of the canyon varies along its length, narrowing from 11 km at the intersection with the continental slope to 3 km at the head near the coast. The eastern boundary of the domain, which represents the coast, is the only closed boundary.

Early model runs employed a 100 km x 100 km domain, however it was found that the domain could be reduced to 70 km x 70 km (moving both the north and south boundaries in 15 km, and moving the western boundary in 30 km) without adversely affecting the solution. The values of $f$ specified in the 70 km x 70 km model domain are appropriate for latitudes between 36° 18.6′ N and 36° 55.6′ N.

High horizontal resolution (1 km x 1 km) is used throughout the domain in order to resolve the motion in the vicinity of the internal tide generation sites and across the narrow canyon. High vertical resolution (30 $\sigma$-levels) is also used throughout the model (Figure 2), in order to accurately resolve the buoyancy frequency profile. The $\sigma$-levels are logarithmically distributed near the surface and bottom, with vertical resolution in the boundary layers ranging from 12.5 m over the basin to 0.5 m over the shelf. In the middle of the water column ($\sigma$-levels 5-26), vertical resolution ranges from 107.5 m over the basin to 4.3 m over the shelf.

The model is initialized with an in-situ temperature and salinity profile that represents summertime stratification conditions in the vicinity of Monterey Bay (Figure 3). The upper 1000 m is the average of 50 CTD casts made near the mouth of Monterey Bay at 36.64° N, 122.14°W (Rosenfeld et al. 1994). Below that, a single cast from August 1993 is used. The same $T$ and $S$ profile is linearly interpolated onto the $\sigma$-coordinates of each grid cell, thus density is initially horizontally homogeneous throughout the domain. Although the equation of state used in POM (described by Mellor 1991) uses potential temperature to calculate in-situ density, the difference between in-situ and potential temperature at 2500 m is negligible for the purposes of this study.

The high horizontal resolution enables the use of very small values for horizontal viscosity. Based on the summary of turbulent diffusion experiments reviewed by Bowden (1962), horizontal

viscosity values of 1-10 $m^2s^{-1}$, corresponding to a Smagorinsky coefficient of 0.01, appear to be appropriate for 1 km resolution. The coefficient of 0.01 was used throughout these experiments. The use of high spatial resolution over the deep basin permits clear identification of regions associated with seaward propagating internal tide energy, however it also necessitates a very short time step in order to ensure model stability (2 s external time step and 120 s internal time step).

*b. Model forcing*

The M2 tide in the eastern Pacific propagates northward with the maximum amplitude at the coast in a manner similar to a barotropic Kelvin wave. Analytical solutions (Munk et al. 1970; Battisti and Clarke 1982) and field studies (Winant and Bratkovich 1981; Rosenfeld and Beardsley 1987) of the barotropic M2 tidal currents in the eastern Pacific are consistent with the Kelvin-like wave comparison, revealing maximum flow (~4 cm $s^{-1}$) parallel to the coast at local high tide and very weak (approximately 1 cm $s^{-1}$ or less) cross-shore flow.

Accounting for the alongshore propagation of the barotropic tide will be important in simulations which incorporate realistic bathymetry beyond the mouth of Monterey Bay. However, in this simplified process study the model was forced at the seaward (western) boundary by specifying the free surface elevation as a cosine wave with a period of 12.4206 h (the M2 period) and an amplitude of 0.5 m, with no variation in the north-south direction. The implications of neglecting alongshore barotropic forcing are considered in the discussion section below. The forcing that was used here is representative of the barotropic M2 tide in Monterey Bay, which essentially co-oscillates (Petruncio 1993, PRP98) with an amplitude of 0.5 m. It will be demonstrated that this forcing produces weak (0.5-1.5 cm $s^{-1}$) barotropic cross-shore currents similar to those observed, but for different reasons. In the model, the surface wave that is reflected from the continental slope and the coastal boundary is approximately 180° out of phase with the incoming tide and has a slightly reduced amplitude due to dissipation through bottom friction (Clarke 1991) and internal tide generation. Thus, currents from this reflected wave nearly cancel currents associated with the

shoreward propagating wave. Observations of the internal tide (PRP98) provide evidence for the appropriateness of a reflective boundary at the coast for the internal modes as well.

Sea level forcing at the western boundary is accomplished by specifying the surface elevation at the boundary as:

$$\eta^{t+1} = R(t) A_{M2} \cos(\omega_{M2}\, t) \qquad (3)$$

where $\eta^{t+1}$ is the surface elevation at the forward time step, *R(t)* is a "ramping" function that increases linearly over each external mode time step from 0 to 1 over an inertial period (and remains equal to 1 thereafter), $A_{M2}$ is the amplitude of the M2 tide (0.5 m), $\omega_{M2}$ is the M2 radian frequency ($1.4052 \times 10^{-1}$ s), and $t$ is the model time, which is incremented each external mode time step. The ramping function is used to reduce the transient oscillations which are generated by starting the model from rest.

For both the external and internal modes, radiation conditions were applied to the north and south boundaries. The internal mode boundary conditions are discussed further in the Appendix.

## 4. Results

Six numerical experiments were carried out, two of which used continental slope/shelf bathymetry with no alongshore variation, while the other four included canyons of various shape (Table 1). All of the experiments involved running the model with tidal forcing in the prognostic mode for four days, with only the last three semidiurnal tidal cycles used for analysis. The cases without alongshore bathymetric variation were conducted in order to assess the generation of internal tides along the continental slope and shelf break, and propagation across a narrow shelf, in the absence of canyons. In addition to confirming previous analytical solutions for internal tide generation, they serve to contrast the results obtained with various canyon shapes. The cases involving canyon geometry were specifically designed to investigate the sensitivity of internal tides to canyon floor slope. Three different floor slopes were investigated, including one which shoals at

an angle that is critical ($\gamma/c = 1$) or near-critical for the M2 frequency along much of its extent. The critically sloping canyon floor is of prime interest, due to its apparent importance in the case of Monterey Canyon and the failure of linear theory to adequately describe critical bottom reflection (Wunsch 1969).

In the remainder of this section, the results of the experiments using simple continental slope/shelf bathymetry are discussed first, and are then contrasted with the canyon case which most closely resembles Monterey Canyon in size and shape. Results of the canyon floor slope investigation are then presented.

*a. Internal Tide Generation Over the Continental Slope and Shelf Break*

The steep continental slope typical of the eastern Pacific was approximated with two different geometric shapes: a linear, 6.62° rise with an abrupt shelf break, and a cosine function with an amplitude of 1200 m and wavelength of 60 km (Figure 4). These runs are referred to as cases 0a and 0b, respectively (Table 1). The cosine amplitude of 1200 m in case 0b was chosen so that the trough of the wave shape would correspond to the onset of the continental rise at a depth of 2500 m, and the crest would occur at the 100 m deep shelf break. The maximum slope resulting from the cosine function was 7.15°, occurring at a depth of 1300 m (the inflection point of the cosine shape). The two shapes are useful in demonstrating the sensitivity of internal tide generation to the rate at which the bathymetry in the generation region transitions from supercritical ($\gamma/c > 1$) to subcritical ($\gamma/c < 1$).

The model results show that the barotropic tidal currents (as represented by the depth-averaged currents) are weak, as expected for a wave that is nearly standing in the cross-shelf direction. Maximum shoreward flow of approximately 1.5 cm $s^{-1}$ occurs, as expected, at the shelf break (Baines, 1983) during rising tide. The increase in barotropic current speed at the shelf break is

a result of the rapid depth change from basin to shelf. It is the vertical velocity induced by the barotropic tidal current flowing over the slope that is the driving force for internal tide generation.

The cross-shelf slices of the current fields during rising tide shown in Figure 4 reveal the relatively strong baroclinic currents resulting from internal tide generation at the shelf break. As discussed by Prinsenberg et al. (1974), who used a modal representation of the current field, the discontinuity in the barotropic cross-shelf velocity at the shelf break results in the generation of two beams of internal waves propagating seaward, and a narrow beam of waves propagating shoreward. These beams can be seen in the cross-shelf velocity snapshots shown in Figure 4. Superimposed on the velocity plots are rays (calculated according to (1) using the initial density profile) indicating the M2 characteristics emanating from the shelf break. As described by Prinsenberg et al., the two characteristics emanating seaward describe the boundaries of the in-phase currents associated with the seaward propagating energy. The lower half of the seaward beam is enhanced by the weak internal tide generation along the continental slope, as discussed in Prinsenberg and Rattray (1975). The presence of several additional beams emanating downward along the continental slope in the case of the cosine-shaped bathymetry can be attributed to the broader area available for internal tide generation, as compared to the linear slope case that represents an abrupt change from supercritical to subcritical bottom slope at the continental shelf break. This result is in agreement with the study of Baines (1974), who found that bathymetric features with concave downward shapes were especially efficient generators of internal tides.

Although not very noticeable in the particular phase of the tide depicted in Figure 4, the base of the 6.62° linear continental slope was also found to be an internal tide generation site. Generation occurred at a depth of approximately 2200 m (where the slope of the M2 characteristic is, over a short depth range, equal to 6.62°) and resulted in a beam of internal tide energy propagating upward and seaward from that generation site. Use of the steeper concave-upward shape at the base of the continental slope was found to nearly eliminate internal tide generation in that portion of the domain. Since internal tide generation at the foot of the continental slope was not the focus of this study, the cosine-shaped continental slope was used for each of the model runs involving canyon

bathymetry. In models with realistic bathymetry, internal wave generation could be expected to occur at various locations along the continental slope, as well as at the shelf break.

By contrast with the offshore-propagating energy, the narrow shelf beam is well-described by a single characteristic reflecting between the sea surface and bottom inshore of the shelf break. A closeup view of the currents between the shelf break and the coast at four points in the tidal cycle is provided in Figure 5. In the case of this abrupt shelf break, the most intense currents are found during rising and falling tides at locations where the beam reflects from the surface and bottom. This was also generally true in the case of internal tides generated at the rounded shelf break, although the beam was slightly more diffuse due to the wider area available for generation.

*b. Monterey Canyon case*

1) CANYON SHAPE

This section discusses the results of a simulation involving a canyon fairly similar to Monterey Canyon in its shape, size, and proximity to the coast, and will be referred to as the Monterey Canyon case or case 1 (Table 1). The bathymetry for this simulation is depicted in Figures 1 and 6. The floor of the real Monterey Canyon increases in depth from 100 m to 1000 m over a distance of approximately 20 km, with an average slope of 2.6°. Its slope is critical with respect to the M2 frequency in the 600-800 m depth range for typical buoyancy frequency profiles. In order to construct a model canyon with its head located near the shore, and ensure realistic width and depth while limiting the steepness of the sides to avoid pressure gradient truncation error (Haney 1991), a canyon floor slope of 1.55° was used. The model canyon head is located 1 km from the closed eastern boundary, and the floor increases in depth from 100 m to 937 m (where it intersects the continental slope) over a distance of 31 km. The rim of the canyon is 11 km wide at the foot, and narrows to 3 km at the head. The canyon floor has a constant width of 3 km. The steepness of the

walls varies. It is no greater than 12.2° at any point, yet it is supercritical for the M2 frequency everywhere. For the initial density profile and the M2 frequency, the model floor slope is critical at a depth of about 300 m.

### 2) CROSS-SHORE (ALONG-CANYON) ENERGY PROPAGATION

As in the previous cases without a canyon, the barotropic currents outside the canyon were found to be strongest at the 100 m deep shelf break, with amplitudes of less than 1.5 cm $s^{-1}$. Within the outer part of the canyon, the depth-averaged current ellipses are similar in magnitude to those on the adjacent outer shelf but more rectilinear (Petruncio 1996). The largest depth-averaged currents (~2 cm $s^{-1}$) are found near the head of the canyon as predicted by Baines (1983).

Vertical sections of the cross-shore currents along the axis of the canyon at four points in the tidal cycle are depicted in Figure 7. The currents associated with the internal tides propagating along the floor of the canyon were found to be 3-4 times stronger than those propagating across the shelf in the case with no canyon (Figure 5). Maximum cross-shore current speeds of 8 cm $s^{-1}$ were found to occur during rising tide, near the critical region of the canyon floor at 300 m depth.

As was observed to be the case in Monterey Canyon during an April 1994 field experiment (PRP98), internal tide energy in the model canyon propagates shoreward nearly parallel to the canyon floor, and downward phase propagation results in maximum shoreward flow occurring later with depth. The linear internal wave characteristic emanating from the foot of the canyon defines the upper boundary of the strongest currents. The phase lag between the model currents and sea level is within 1/4 cycle of that reported by PRP98 for the April conditions; near the head of the canyon, maximum shoreward flow occurs in the lower half of the water column, close to the time of high tide. The observed semidiurnal currents and the model currents derived using M2 forcing are depicted at similar phases in Figure 8. Although the model currents are 50% weaker than those observed, the structure of the observed and modeled current fields are similar, with strong shoreward flow along the floor, offshore flow near the surface, and isophase lines nearly parallel to the canyon floor.

The region of strongest current activity in the model simulation lies in the bottom boundary layer, at floor depths of 200 to 300 m. Inspection of the density field in this boundary layer (Figure 9) reveals the presence of bore-like surges along the canyon floor. A thin layer of dense water is seen to surge up the floor during rising tide, resulting in isopycnal displacements of 5-10 m. At these depths, the vertical resolution in the bottom three $\sigma$-levels is between 1 and 1.5 m. This boundary layer activity is consistent with the 2-D numerical simulations of Slinn and Riley (1996), who observed that critical angle internal wave reflection on floors with shallow slopes (3.4°-9°) resulted in the upslope propagation of thermal fronts in the bottom boundary layer.

The specified tidal forcing is monochromatic and, although nonlinear interactions can give rise to other frequencies (Xing and Davies 1996), most of the energy remains in the semidiurnal band. Therefore, the amplitudes of the M2 tidal currents ($u_0$, $v_0$, $w_0$) and density ($\rho_0$) oscillations are estimated directly from the variance fields, since this method is less computationally intensive than using a least squares harmonic analysis for the M2 frequency at each grid point. To estimate the M2 amplitudes, the $u$, $v$, $w$, and $\rho$ fields, sampled at an interval of 3720 s (12 points per tidal cycle), were demeaned and the resulting perturbation quantities (e.g., $A'$) used to compute amplitudes according to $A_o = (2\overline{A'^2})^{\frac{1}{2}}$, where the overbar denotes the mean value over three tidal cycles. We found that amplitudes calculated in this manner were practically identical to those arrived at from the harmonic analysis method of Foreman (1978).

In order to observe the effects of the internal tide on the near-surface and near-bottom currents, the shallowest (between $\sigma$-levels 1 and 2 at 0.27-6.75 m) and deepest (between $\sigma$-levels 29 and 30 at 0.27-6.75 m above the bottom) tidal ellipses are shown in Figure 10. The near-surface ellipses 5 to 10 km south of the canyon are amplified 5-10 times above their barotropic values. This is where beams emanating from the southern canyon rim reflect from the surface. This pattern is in general agreement with HF radar-derived tidal ellipses for Monterey Bay (PRP98), although the near-surface ellipses directly over the head of the model canyon are only slightly amplified above their barotropic values.

Within the model canyon, progressing toward shore, the near-bottom currents significantly strengthen at a depth of 300-350 m in the critically sloping region about 8 km from shore. The near-bottom currents are also intensified over the southern rim of the canyon, where significant internal tide generation is observed to occur.

Thus far we have looked at model results in terms of the amplitude of the tidal currents produced in the simulations. Velocity, however, is not the quantity most representative of the energy conversions taking place between the barotropic forcing and the baroclinic internal tides. Therefore, the energetics associated with the internal tide were investigated by calculating the mean perturbation kinetic energy density, KE = $(\frac{1}{4}\rho_0\left(u_0^2 + v_0^2 + w_0^2\right))$ and potential energy density, PE = $(\frac{1}{4}\frac{g^2\rho_0'^2}{\rho_0 N^2})$ on along- and cross-canyon slices. For these computations, $N$ was computed from the vertical gradient of the model mean density field calculated over 3 tidal cycles, using centered differencing between $\sigma$-levels. The vertical velocity used in calculating KE was first converted from $\sigma$ to $z$-coordinates according to:

$$w = w_\sigma + U\sigma\frac{\partial D}{\partial x} - \frac{\partial \eta}{\partial x} + V\sigma\frac{\partial D}{\partial y} - \frac{\partial \eta}{\partial y} + \left(\sigma\frac{\partial D}{\partial t} + \frac{\partial \eta}{\partial t}\right), \qquad (9)$$

where $w_\sigma$ is the vertical velocity referenced to $\sigma$-coordinates, $\sigma$ is the value of the $\sigma$-coordinate for the grid cell of interest, $D$ is the total depth (bathymetric depth plus free surface elevation) and $\eta$ is the free surface elevation (Blumberg and Mellor 1987). In this application however, the horizontal gradients of $\eta$ are negligible and were not included. Once computed, KE and PE were summed to obtain the mean perturbation total energy per unit volume (E).

Figure 11 shows $u_0$ and E in a slice along the canyon. Maximum values occur near the floor close to the canyon head. A "shadow zone" of minimal internal tide energy exists between the M2 characteristic rays emanating shoreward from the foot of the canyon and the reflected ray descending from the sea surface near the canyon head to the floor of the deep basin. The increase in E with depth is consistent with the E profiles calculated from both the April and October field

measurements reported by PRP98. However, the maximum value of 2.1 J $m^{-3}$ is 25-50% of the observed magnitudes. Qualitative agreement with the measurements was also found in the ratio of PE to KE. PE was found to be greater than KE near the head of the model canyon, as was the case in the real canyon. Linear theory, on the other hand, predicts a PE:KE ratio of 1:2.26 for the M2 frequency at this latitude. The observed and modeled skewing of the energy distribution towards more PE may be related to internal wave shoaling near the canyon head, although this speculation requires further study.

E in five cross-canyon slices, obtained every 6 km between 26 km and 2 km from shore, are depicted in Figure 12. Progressing shoreward from the deepest slice 26 km from shore, E is seen to be focused near the floor (as was found to be the case in the along canyon slices), but is asymmetrically distributed in the cross-canyon direction, with a greater percentage lying along the southern wall. This asymmetry in energy distribution is likely due to rotational effects, and is discussed further in Section 5. Local internal tide generation along the canyon floor is expected where the floor slope is critical for the M2 frequency, which occurs at a depth of about 300 m and 8 km from shore. Indeed, the internal tide appears to be much more energetic in the final 2 slices 8 km and 2 km from shore, and energy near the floor is more symmetrically distributed.

In order to observe changes in total internal tide energy in the cross-canyon slices, it is a simple matter to multiply values of E by the average vertical and horizontal thicknesses of the corresponding $\sigma$-cells and sum over the slice, using the 1 km model resolution for the cross-shore dimension. Given the E distributions seen in Figure 12, particularly near shore, it is important to include the energy associated with the waves generated along the rims within these volume segments, since they may represent a transfer of energy from internal tides propagating along canyon to those propagating along the coast. A cross-canyon (along-shore) segment width of 31 km was therefore chosen so that contributions from the rim-generated waves would be included in the calculation. The total energy in each volume segment is depicted in Figure 13 along with similar computations for the additional canyon cases discussed below.

In case 1, the total perturbation energy in the vicinity of the canyon decreases between the volume segments centered 26 km and 14 km from shore. This energy decrease most likely represents turbulent dissipation of the internal tide due to shear along the canyon floor and walls. The total energy present in the vicinity of the canyon nearly doubles however, between segments centered 14 km from shore and 8 km from shore, indicating that contributions from internal tide generation on the floor of the canyon far outweigh the losses due to dissipation. It should be noted that if the floor slope served only to focus the energy associated with the shoreward propagating internal tide into a decreasing cross-sectional area, the total baroclinic energy present would either remain constant, or decrease due to turbulent losses in the bottom boundary layer. However, the critical floor slope also provides a generation site for internal tides; energy is therefore transferred from the barotropic tide to the baroclinic tide not only at the foot of the canyon but along the floor in the upper reaches of the canyon as well.

### 3) Along-Shore Energy Propagation

Energy transfer is also likely to occur along the canyon rims. Significant isopycnal displacements associated with the internal tides are observed near the rims of the canyon close to the head of the model canyon (Figure 14). As the strong shoreward flow encounters the head of the canyon, isopycnal displacements of 5 to 10 m move water from beneath the canyon rim up onto the shelf. As the isopycnals sink back down below the rim, lenses of dense water pinch off and remain on the shelf, in the manner suggested by Shea and Broenkow (1982). Based on observations from Monterey Canyon, Shea and Broenkow consider this process a potentially significant source of nutrient enrichment for Monterey Bay.

This “tidal pumping” along the rim of the model canyon near its head is clearly a source of along-shore-propagating internal tides. Evidence for this is seen in the cross-canyon E sections in Figure 12. A snapshot of the along-shore velocity component in an along-shore slice near the head of the canyon is depicted in Figure 15. This was taken from an early model run using the larger 100

km x 100 km domain, which provides a better view of the gradual change of the along-shore internal tide from beam-like near the generation site at the canyon rims to first-mode-like near the model boundaries. The surface and bottom reflections of the beams emanating from the north rim of the canyon are regularly spaced and, after the second surface reflection, visual inspection indicates that most of the higher modes have been damped out. The remaining signal propagates as a first vertical mode internal Kelvin wave. The signature of these waves can be seen in surface current patterns, as well as in small (3-4 mm) deflections of the sea surface, that decay exponentially offshore over a distance of 4 km, which is approximately one internal Rossby radius of deformation. The northward alongshore phase speed of 35 cm $s^{-1}$, estimated from successive plots of free surface elevation, is very close to the theoretical value of $(g'H)^{\frac{1}{2}}$ = 37.8 cm $s^{-1}$.

The beams of internal tide energy in Figure 15 projecting southward from the canyon rim are slightly more intense and appear less regularly spaced. The irregular spacing is probably due to the fact that the waves on the south side of the canyon are not propagating along the coast, but are propagating seaward across the shelf as ordinary internal Poincare waves. The sea surface signature of these waves is much broader and indicates a radial spread of internal wave energy away from the canyon. This interpretation of the north-south asymmetry in wave generation and propagation is supported by model runs with the Coriolis parameter set to zero (i.e., no rotation). In the absence of rotation, the waves have no preferential direction of propagation. Instead, symmetric generation of internal waves along the rims of the canyon and radial spreading of internal wave energy away from the canyon head are observed.

*c. Effect of canyon floor slope*

In order to further investigate the effects of canyon floor slope on internal tide propagation, additional experiments were conducted with bottom slopes of 0.74°, 1.55°, and 2.29° (cases 2a, 2b,

and 2c, respectively, Table 1). In all three cases, V-shaped canyons with width constant along the length (3 km at the floor and 11 km at the rim) were used (Figure 16). Due to the fact that the ratio $\gamma : c$ at the bottom of the water column varies along the length of the canyons (since $N$ is a function of depth), the two steepest model floor slopes cannot be strictly defined as either subcritical, critical, or supercritical. The 0.74° floor slope however, is subcritical along its entire length.

The mean perturbation energy density, E, was calculated for along-canyon and cross-canyon slices as described in the previous section. Looking first at the along-canyon comparisons in the region of the canyon (Figure 17), we see that the largest energy density is found along the floor in the case of the 1.55° floor slope. The peak value occurs where the floor slope is parallel to the linear internal tide ray path (cf Figure 11). In the more steeply sloping case with a floor slope of 2.29°, there is a broad region near the floor with large energy densities, particularly in the deep water at the foot of the canyon. In the 0.74° and 1.55° cases, the foot of the canyon represents a change from supercritical to subcritical bathymetry, while in the 2.29° case this change is from supercritical to critical. The transfer of energy from the barotropic tide to the baroclinic tide is, therefore, accomplished more efficiently with the 2.29° floor slope, since the barotropic motion (guided by the floor slope) and the baroclinic motion (guided by the frequency of the forcing and the degree of stratification) lie in the same plane. However, little of the energy generated at the foot of the 2.29° canyon floor reaches the shelf, since the floor is supercritical for the M2 frequency at shallower depths. Finally, the 0.74° floor slope results in relatively low E values since it is subcritical with respect to the M2 frequency along its entire length.

E along three cross-canyon slices are presented for each of the constant width canyons in Figure 18. Note that the vertical scale used to depict the slice at a given offshore location is kept the same for each of the three canyons, but the scale changes between offshore locations. Due to the short length of the canyon with the 2.29° floor slope, the slice closest to shore (2 km from shore) actually represents the portion of the continental shelf which lies shoreward of that canyon, and illustrates the minor amount of baroclinic energy reaching the shelf in that case. The distribution of E in each of the three canyons shows some evidence of trapping along the south wall. Total energy

estimates for these three cases are also depicted in Figure 13. These curves show that the amount of energy present near the foot of the canyon with the 2.29° floor slope is more than twice that present in the other canyons, but that little of that energy reaches the inner shelf. The increase in energy that occurs between 14 km and 2 km from shore with the 0.74° floor slope (case 2a) most likely indicates some contribution from generation along the canyon rim. The contribution of energy from that process is apparently sufficient to offset turbulent losses in the bottom boundary layer. The energy in the 1.55° floor slope case also increases between 14 km and 2 km from shore, however this increase is larger than in the subcritical case, due to an additional contribution from generation along the critically sloping floor in the vicinity of 8 km from shore as was seen in case 1.

## 5. Discussion

### *a. Trapped internal wave theory*

Linear theory for freely propagating and standing internal waves is reviewed in PRP98. Here we discuss theory relating to trapped, or evanescent, internal waves since our results indicate their presence. The effect of canyon walls on internal tide propagation has been discussed in traditional 2-D terms, i.e. as either subcritical or supercritical for internal waves incident from above (Gordon and Marshall 1976; Hotchkiss and Wunsch 1982). Hotchkiss and Wunsch state that the effect of sloping walls in a V-shaped canyon is to enhance the focal properties of canyons so that energy entering the canyon from above will tend to be concentrated near the floor. Hotchkiss and Wunsch also consider the effect of internal tide generation at the rim of a canyon, noting that beams of energy should radiate toward both the shallow and deep water (i.e., up onto the shelf, and down into the canyon). Another possible effect which has not received attention in the literature is that energy propagating shoreward in a canyon can become trapped along the right side of the canyon (facing shoreward), if certain conditions are met (Rhines 1970).

Rhines (1970) presents a theoretical treatment of inertia-gravity wave propagation which includes the combined effects of stratification, rotation, and topography based on linearized, Boussinesq equations for wave motion in a rotating, stratified fluid bounded by a single wall. Rhines shows that edge waves may occur for all frequencies less than $N \sin \gamma_w$, where $\gamma_w$ is the angle of the inclined wall from the horizontal. Rotational effects cause the waves to propagate with shallow water to the right, however the maximum trapping frequency is independent of $f$. The frequency of the trapped waves and their angle of propagation are related to the inclination angle by $\omega = N \sin \gamma_w \sin \phi$, where $\phi$ is the angle between the upslope direction and the horizontal component of the phase velocity. The degree of trapping (i.e., the proximity to the wall of significant motion) is shown to be strongly dependent on $\gamma_w$ and its relation to a trapping coefficient $S = N/f$. In the limiting case of a vertical wall, the edge wave is simply an internal Kelvin wave, with motion decaying exponentially away from the wall. For relatively small slopes ($\gamma_w \sim S^{-1}$) and $\omega \sim f$, the case most applicable to internal tide propagation, strong trapping occurs, with motion penetrating about one wavelength into the fluid. In this case, the "wall" is more appropriately described as the bottom, and the waves are referred to as "bottom-trapped" waves. As in the case of free internal tides propagating normal to the depth contours, planes of constant phase for the bottom-trapped waves are almost parallel to the boundary. Rhines speculates that the semidiurnal barotropic tide incident on the continental rise could produce strong trapped motions propagating energy along the isobaths (i.e., along the continental slope), as well as the more commonly discussed free waves.

In the Monterey Canyon case experiment (case 1), conditions are favorable ($\omega_{M2} < N \sin \gamma_w$) for trapping the internal tide along the southern wall in the middle and deeper parts of the canyon. Examination of perturbation energy in cross-canyon slices of the model data does in fact reveal asymmetric energy distribution (Figures 12 and 18), with greater energy density existing along the southern wall of the canyon. It is also found that generation of internal tides at the rim of the canyon is asymmetric, with stronger generation occurring along the southern rim.

Generation of internal tides at the rim of a canyon could be caused by the vertical components of both the barotropic and baroclinic tidal currents, however the vertical component of

the baroclinic tides encountering the rim of this model canyon would be an order of magnitude stronger than that of the barotropic tide. The horizontal components of the barotropic tidal currents near the head of this model canyon are only a few millimeters per second, and the vertical component induced by the sloping sides of the canyon would be even smaller. The fact that internal tide generation is stronger on the southern rim of the model canyon is in accordance with the increased baroclinic energy already present along the southern wall due to trapping of shoreward propagating internal tides. In the real ocean, a greater contribution to internal tide generation by the horizontal component of the barotropic tide would be expected in canyons which are not sheltered by a bay, and which are thus exposed to stronger alongshore (cross-canyon) barotropic currents.

***b. Comparison with prior idealized study of Baines (1983)***

Some aspects of the present study are similar to the combined laboratory and analytical work described by Baines (1983) in which a constant-slope, constant-width, narrow canyon was simulated. In that study, the strengths, phases, and reflection conditions of internal tides generated within the idealized canyon were also sensitive to the ratio $\gamma / c$. The laboratory results were dominated, however, by reflections from the open boundary at the foot of the canyon leading to down-canyon energy propagation, particularly in the critical case, $\gamma / c = 1$. We do not see that in our primitive equation simulations. Differences in canyon geometry and stratification between our study and that of Baines (1983) may explain this difference in behavior. Our canyon floor slopes are small compared with the continental slope, whereas the canyon floor and continental slope have identical steepnesses in the Baines study. As a result, there is no equivalent to the canyon foot generation site in the earlier work.

Because of the variable buoyancy profile employed in our case, we have focused on the importance of local internal tide generation where the floor slopes are critical for only a few kilometers. That is, $\gamma / c$ is spatially variable within a run. Multiple generation sites, such as the canyon foot and the locally critical floor region, can produce complex interactions and affect the internal tide phases to some degree, but we see upward (shoreward) energy propagation along the

bottom in all cases. Hence, reflections of the baroclinic motions from our model coastal boundary---and from supercritical portions of the canyon floor---are important, but they result in depth-concentrated (high-mode) reflections that do not resonate with the offshore open boundary in the manner reported by Baines (1983).

***c. Comparison to observations***

Figure 8 depicts snapshots of the semidiurnal currents observed in Monterey Canyon and the model-derived M2 currents for the idealized canyon shape. Although the model currents are 50% weaker than observed, the structure of the observed and modeled current fields are qualitatively similar, with strong shoreward flow along the floor and offshore flow near the surface. In both cases, the isophase lines are nearly parallel to the canyon floor.

There are several reasons why the model currents might be expected to be weaker than the baroclinic tidal currents observed in Monterey Canyon. One is the simplified model bathymetry. The only internal tides entering the model canyon are those generated at the foot, along the floor, and on the rims. In the real ocean one may expect to find features seaward of a canyon which also generate internal tides and further contribute to the amount of internal tide energy focused by the canyon. Such is the case in Monterey Bay, where a large feature ("Smooth Ridge") favorable for internal tide generation lies just seaward of Monterey Canyon (PRP98). The strength of the internal tides generated at a given site is affected by the depth of the generation site, since for a given cross-shelf barotropic mass flux, the barotropic current speeds will be greater above a shallow shelf break than a deeper one. Also, the complicated shape of the shelf break in the vicinity of Monterey Bay may result in propagation of internal tide energy into Monterey Canyon from other shallow generation sites.

Secondly, some of the disparity between the strength of the modeled and observed internal tides can also be attributed to the use of only one tidal constituent in the model. This simulation was forced with a sea level amplitude of 0.5 m, corresponding to the M2 tidal constant amplitude of 0.5

m measured in Monterey Bay. The April 1994 measurements described in PRP98 were made during a time of spring tides when the observed tidal range, a result of superposition of tidal constituents not separable in a 25 h time series, was closer to 1 m. A model simulation forced with 1 m M2 amplitude (simulating superposition of several semidiurnal tidal constituents) results in a model current field with similar vertical structure but maximum amplitudes of 15 cm $s^{-1}$, much closer to the observed 20 cm $s^{-1}$ internal tide amplitude.

Thirdly, it is noted that the barotropic tidal currents in the Eastern Pacific, seaward of Monterey Bay, have a significant along-shore (hence, cross-canyon) component, which could generate significant internal tides along the canyon rims and at other topographic features which lie beyond the mouth of the Bay. This additional internal tide generation could contribute significantly to the internal tide energy levels within Monterey Canyon. The model's barotropic tidal current is purely cross-shore. Finally, the presence of upwelling plumes, fronts, and eddies near Monterey Bay may modify the propagation paths of internal tide energy, and could serve to focus additional energy into Monterey Canyon. The initial horizontal homogeneity of the model density field precludes this possibility.

Once generated, the internal tidal currents propagating within the model canyon are influenced by their interactions with the turbulent boundary layers. Therefore, some aspects of these results, such as the magnitude of the currents within the canyon and the amount of tidal pumping along the canyon rims, will depend on the details of the turbulence closure scheme and accompanying model coefficients. Only the standard POM closure scheme was used in this study (Mellor and Yamada, 1982). Future studies would benefit from a sensitivity study to a wider variety of turbulence coefficients, as performed recently by Holloway and Barnes (1998). Even more appropriate may be simulations using a variety of turbulence closure schemes, as employed by Allen et al. (1995) in two-dimensional simulations of coastal upwelling fronts.

## 6. Conclusions

This study, using the Princeton Ocean Model with 30 $\sigma$-levels in the vertical and 1 km x 1 km horizontal resolution, demonstrates that internal tide generation can occur at the foot, floor, and rims of a submarine canyon, when forced with 0.5 m amplitude semidiurnal sea level oscillations along the offshore boundary. The baroclinic tidal currents in the model dominate the barotropic tidal currents, which have weak cross-shore components. This situation is typical of the central California coast and other coastal regions with narrow continental shelves.

Tidal forcing in the presence of a continuously stratified density field results in internal tide energy propagation along paths that are well described by the characteristic slopes given by the linear dispersion relation for internal waves. Beams of energy are observed to propagate shoreward and seaward from the shelf break and from the canyon foot. The strength of the internal tides propagating shoreward in model canyons, and the amount of internal tide energy reaching the canyon head, are found to be very sensitive to canyon floor slope. Specification of a 1.55° floor slope, which is slightly subcritical for the M2 frequency near the foot of the canyon and critical in the upper reaches of the canyon, results in a bottom-intensified internal tide which propagates energy along the length of the canyon from the foot to the head (Figure 11). In this case, internal tide generation is observed to occur not only at the canyon foot but also along the critically sloping portion of the canyon floor, and on the rims of the canyon near the canyon head as well. Generation along the floor results in a significant contribution to total perturbation energy within the model canyon, however the strong currents associated with generation along the floor appear to be confined to a thin bottom boundary layer. The importance of internal tide generation along the floors of real canyons, which are not as straight and smooth as the model canyon floor, remains to be established.

A minor reduction in floor slope (from 1.55° to 0.74°), such that the canyon floor is subcritical for the M2 frequency along its entire length, results in much weaker canyon currents (1.5 cm $s^{-1}$ versus 8 cm $s^{-1}$) and virtually no generation of internal tides along the canyon rims. A minor

increase in floor slope (from 1.55° to 2.29°), such that the canyon floor is critical at the foot and supercritical near the head, results in much more energy near the foot, but much less energy shoreward of the canyon head due to backward reflection of the internal tide energy in the upper reaches of the canyon (Figure 17).

The vertical motions associated with the internal tide near the head of the model canyon result in pumping of cold water from the canyon onto the shelf (Figure 14), as suggested by Shea and Broenkow (1982) based on observations from Monterey Canyon. Bottom-trapping (Rhines 1970) may result in a focusing of shoreward-propagating internal tide energy along the southern wall of the model canyons. This may also result in stronger generation of internal tides and greater pumping of cold water along the southern rim near the canyon head. Relatively strong internal tide generation is observed to occur along the canyon rims near the head, with subsequent propagation of internal tides in the alongshore direction (Figure 15). Trapping due to rotational effects was also observed in these alongshore-propagating internal tides, which propagate as internal Kelvin waves north of the canyon but are more diffuse on the south side.

Upward propagation of internal tide energy from the canyon rims, and the subsequent reflection of this energy from the sea surface, results in amplification of surface currents near the canyon head. This mechanism for enhancement of surface tidal currents may explain observations of stronger semidiurnal surface currents above the head of Monterey Canyon (Paduan and Cook 1997; PRP98).

Despite the use of simplified bathymetry and tidal forcing, the numerical simulations reproduce several features of the internal tide that are in qualitative agreement with observations in Monterey Canyon, including upcanyon energy propagation, bottom-intensified currents above the canyon floor, internal tide generation along the rim of the canyon, and tidal pumping of dense water up onto the shelf near the canyon head. The fact that these features are observed in the presence of simplified bathymetry and forcing is encouraging for the future use of this model as a numerical laboratory to simulate internal tide generation and propagation in the presence of realistic bathymetry and, indeed, large efforts are underway to use realistic numerical modeling to assess the

role of barotropic-to-baroclinic energy conversion along continental margins (Cummings and Oey, 1997), at the Hawaiian Ridge (Kang et al., 2000; Merrifield and Holloway, 1999; Luther, 1999), and associated with particular features such as the Monterey Submarine Canyon (Rosenfeld et al., 1999).

*Acknowledgments*. The authors would like to thank Mike Cook for his assistance with all aspects of this research. Drs. P Chen, R. Haney, J. Lewis, and R. Signell offered valuable advice on the use and/or visualization of the POM. We gratefully acknowledge support by the Office of Naval Research in the form of a Graduate Fellowship for Dr. Petruncio and contract N0001497WR30009 to Drs. Paduan and Rosenfeld. The Naval Postgraduate School provided time on their Cray computer, and the Monterey Bay Aquarium Research Institute supported Dr. Rosenfeld during some of the time she worked on this project.

APPENDIX

## Internal Mode Boundary Conditions

The formulation of boundary conditions for internal waves is an area of active research. The simplest approach is to apply a sponge boundary condition in which the velocity is gradually reduced to zero over a number of model grid points. There are a number of drawbacks to sponge boundaries, however, including greater computational expense (as compared to a radiation condition) due to the requirement for a larger domain, and the prevention of two-way information flow that is desirable in nested grid systems. A more physically correct, but computationally complex, approach is to decompose the baroclinic mode velocities into a set of internal orthogonal modes and prescribe boundary conditions for each mode (Shulman and Lewis 1995). If the internal waves in the model domain are propagating mainly in the first baroclinic mode, a simplified radiation condition can be formulated based on the approximate phase speed of the first mode wave, $c_i \approx (g'H)^{1/2}$. This approximation can be incorporated into the explicit gravity wave radiation condition (Chapman 1985):

$$U_B^{t+1} = \mu\, U_{B\pm1} + (1-\mu) U_B^t, \qquad \text{(A1)}$$

where $\mu = c_i \Delta t / \Delta x$.

If the phase speed of the internal waves is improperly specified (via the μ term in the radiation boundary condition), only partial transmission of the internal waves through the boundary will occur. In our case, initially imperfect transmission was detected in animations of sea level, which depicted internal Kelvin waves propagating along the closed eastern boundary and then turning the corner (as if the open boundary were closed) and propagating westward with a slightly reduced amplitude. The model domain size was subsequently chosen such that the internal Kelvin waves would be propagating in the first mode by the time they encountered the open boundary, and the phase speed of a first mode wave was used in the formulation of the radiation boundary condition.

The choice of $\Delta x$ =1 km (constant throughout the domain), $\Delta t_i$ =120 s, and the estimated maximum internal phase speed of $c_i \approx (9.8 \times \frac{0.15}{1027} \times 2500)^{\frac{1}{2}} = 1.89$ m s$^{-1}$ results in $\mu_{MAX}$ = 0.227. $\mu$ is assumed to vary only with water depth (the density perturbation is assumed to be constant along the boundary), and is therefore approximated by $\mu \approx 0.227\left(H / H_{MAX}\right)^{1/2}$. This approximation is successfully applied on the north and south boundaries of the domain.

This approximation is not suitable at the western boundary, where the internal tide is propagating in a beam-like manner (i.e., in many modes). A sponge boundary condition is therefore employed at the western boundary. The internal velocity components are gradually reduced to zero at the western boundary through multiplication with the sponge, which is defined as:

$$SP = 1 - [1 - \left( \frac{i-2}{N} \right)]^2 \qquad \text{(A2)}$$

where $i$ is the grid point number (increasing in the eastward direction from 1 to $i_{MAX}$) and $N$ is the total number of grid points used for the sponge, which in this case is 10.

## REFERENCES


Allen, J. S., P. A. Newberger, and J. Federiuk, 1995: Uwpelling ciculation on the Oregon continental shelf. Part I: Response to idealized forcing. *Journal Physical Oceanography*, **25**, 1843-1866.

Baines, P. G., 1974: The generation of internal tides over steep continental slopes. *Philos. Trans. Roy. Soc. London*, **277,** 27-58.

Baines, P. G., 1982: On internal tide generation models. *Deep-Sea Res.*, **21,** 307-338.

Baines, P. G., 1983: Tidal motion in submarine canyons - a laboratory experiment. *J. Phys. Oceanogr.*, **13,** 310-328.

Battisti, D. S. and A. J. Clarke, 1982: A simple method for estimating barotropic tidal currents on continental margins with specific application to the M2 tide off the Atlantic and Pacific Coasts of the United States. *Journal Physical Oceanography*, **12,** 8-16.

Blumberg, A. F. and L. H. Kantha, 1985: Open boundary conditions for circulation models. *J. Hydraulic Eng.*, **111,** 237-255.

Blumberg, A. F. and G. L. Mellor, 1987: A description of a three-dimensional coastal ocean circulation model. *Three-Dimensional Coastal Ocean Models*, Vol. 4, N. Heaps, Ed., American Geophysical Union**,** 1-16.

Bowden, K. F., 1962: Turbulence. *The Sea*, Vol. 1, M. N. Hill, Ed., John Wiley and Sons**,** 802-825.

Chapman, D. C., 1985: Numerical treatment of cross-shelf open boundaries in a barotropic coastal ocean model. *Journal Physical Oceanography*, **15,** 1060-1075.

Clarke, A. J., 1991: The dynamics of barotropic tides over the continental shelf and slope. *Tidal Hydrodynamics*, B. B. Parker, Ed., John Wiley and Sons, Inc.**,** 79-107.

Cummins, P. F. and L.-Y. Oey, 1997: Simulation of barotropic and baroclinic tides off northern British Columbia. *Journal Physical Oceanography*, **27,** 762-781.

Foreman, M. G. G., 1978: Manual for tidal currents analysis and prediction. Inst. Of Ocean Sciences, Patricia Bay Pac. Mar. Sci. Rep. 78-6, 70 pp.

Foreman, M. G. G., 1995: Tide removal requiring a dynamical interpretation. *Quantitative Skill Assessment for Coastal Ocean Models*, D. R. Lynch and A. M. Davies, Eds., Amer. Geophys. Union**,** 224-239.

Galperin, B. and G. L. Mellor, 1990: A time-dependent, three-dimensional model of the Delaware Bay and River system, part 1: description of the model and tidal analysis. *Estuarine, Coastal, and Shelf Sci.*, **31,** 231-253.

Gordon, R. L. and N. F. Marshall, 1976: Submarine canyons: internal wave traps? *Geophys. Res. Lett.*, **3,** 622-624.

Haney, R. L., 1991: On the pressure gradient force over steep topography in sigma coordinate ocean models,. *Journal Physical Oceanography*, **21,** 610-619.

Holloway, P. E., 1996: A Numerical Model of Internal Tides with Application to the Australian North West Shelf. *Journal Physical Oceanography*, **26,** 21-37.

Holloway, P. E., and B. Barnes, 1998: A numerical investigation into the bottom boundary layer flow and vertical structure of internal waves on a continental slope. *Cont. Shelf Res*., **18**, 31-65.

Hotchkiss, F. S. and C. H. Wunsch, 1982: Internal waves in Hudson Canyon with possible geological implications. *Deep-Sea Res.*, **29,** 415-442.

Huthnance, J. M., 1989: Internal tides and waves near the continental shelf edge. *Geophys. Astrophys. Fluid Dyn.*, **48,** 81-106.

Kowalik, Z. and T. S. Murty, 1993: *Numerical Modeling of Ocean Dynamics*. Advanced Series on Engineering. World Scientific, 481 pp.

Kang, S.K., M.G.G. Foreman, W.R. Crawford, and J.Y. Cherniawsky, 2000: Numerical modeling of internal tide generation along the Hawaiian Ridge. *Journal Physical Oceanography*, **30**, 1083-1098.

Lewis, J. K., Y. L. Hsu and A. F. Blumberg, 1993: Boundary forcing and a dual mode calculation scheme for coastal tidal models using step-wise bathymetry. *Proc. ASCE 3rd International Estuarine and Coastal Modeling Conference*, Sponsored by the Waterway, Ports, Coastal and Ocean Division, 422-431.

Luther, D., 1999: The Hawaiian Ocean Mixing Experiment (HOME). *Proceedings, 'Aha Huliko'a Hawaiian Winter Workshop*, University of Hawaii at Manoa, 19-22 January, pg 57-62.

Mellor, G. L., 1991: An equation of state for numerical models of oceans and estuaries. *J. Atmos. Oceanic Technol.*, **8,** 609-611.

Mellor, G. L., 1996: User's guide for a three-dimensional, primitive equation, numerical ocean model. Atmospheric and Ocean Sciences Program, Princeton Univ. Unpublished Report.

Mellor, G. L., and T. Yamada, 1982: Development of a turbulence closure model for geophysical fluid problems. *Reviews of Geophysics and Space Physics*, **20**, 851-875.

Mellor, G. L., T. Ezer and L.-Y. Oey, 1994: The pressure gradient conundrum of sigma coordinate ocean models. *J. Atmos. Oceanic Technol.*, **11,** 1126-1134.

Merrifield, M.A., and P.E. Holloway, 1999: Internal tide generation at open ocean topographies. *Proceedings, 'Aha Huliko'a Hawaiian Winter Workshop*, University of Hawaii at Manoa, 19-22 January, pg 51-56.

Munk, W., F. Snodgrass and M. Wimbush, 1970: Tides offshore: transition from California coastal to deep-sea waters. *Geophys. Fluid Dyn.*, **1,** 161-235.

Munk, W., and C. Wunsch, 1998: Abyssal recipes II: energetics of tidal and wind mixing. *Deep-Sea Res.*, **45**, 1977-2010.

O'Connor, W. P., 1991: A numerical model of tides and storm surges in the Rio de la Plata Estuary. *Cont. Shelf Res.*, **11,** 1491-1508.

Oey, L.-Y. and P. Chen, 1992: A model of circulation in the Northeast Atlantic shelves and seas. *J. Geophys. Res.*, **97,** 20,087-020,115.

Oey, L.-Y., G. L. Mellor and R. I. Hires, 1985: A three-dimensional simulation of the Hudson-Raritan Estuary, part I: description of the model and model simulations. *Journal Physical Oceanography*, **15,** 1676-1692.

Oey, L.-Y., Y.-H. Zhang and P. Chen, 1992: Simulation of the Norwegian Coastal Current in the vicinity of the Halten Bank: comparison with observations and process study of bank-induced meanders. *J. Mar. Sys.*, **3,** 391-416.

Paduan, J. D. and M. S. Cook, 1997: Mapping surface currents in Monterey Bay with CODAR-type HF radar. *Oceanography*, **10,** 49-52.

Perénne, N., J. Verron, D. Renouard, D.L. Boyer, and X. Zhang, 1997: Rectified barotropic flow over a submarine canyon. *Journal Physical Oceanography*, **27**, 1868-1893.

Petruncio, E. T., 1993: Characterization of tidal currents in Monterey Bay from remote and in-situ measurements. M.S. thesis, Dept. of Oceanography, Naval Postgraduate School, 113 pp.

Petruncio, E. T., 1996: Observations and modeling of the internal tide in a submarine canyon. Ph.D. dissertation, Dept. of Oceanography, Naval Postgraduate School, 181 pp.

Petruncio, E. T., L. K. Rosenfeld and J. D. Paduan, 1998: Observations of the internal tide in Monterey Canyon. *Journal Physical Oceanography*, **28**, 1873-1903**.**

Polzin, K. L., J. M. Toole, J. R. Ledwell and R. W. Schmitt, 1997: Spatial variability of turbulent mixing in the abyssal ocean. *Science*, **276,** 93-96.

Prinsenberg, S. J. and J. M. Rattray, 1975: Effects of continental slope and variable Brünt-Väisälä frequency on the coastal generation of internal tides. *Deep-Sea Res.*, **22,** 251-263.

Prinsenberg, S. J., W. L. Wilmot and J. M. Rattray, 1974: Generation and dissipation of coastal internal tides. *Deep-Sea Res.*, **21,** 263-281.

Rhines, P., 1970: Edge-, bottom-, and Rossby waves in a rotating stratified fluid. *Geophys. Fluid Dyn.*, **1,** 273-302.

Rosenfeld, L. K. and R. C. Beardsley, 1987: Barotropic semidiurnal tidal currents off northern California during the Coastal Ocean Dynamics Experiment (CODE). *J. Geophys. Res.*, **92,** 1721-1732.

Rosenfeld, L.K., J.D. Paduan, E.T. Petruncio, and J.E. Goncalves, 1999: Numerical simulations and observations of the internal tide in a submarine canyon. *Proceedings, 'Aha Huliko'a Hawaiian Winter Workshop*, University of Hawaii at Manoa, 19-22 January, pg 63-71.

Rosenfeld, L. K., R. E. Schramm, J. B. Paduan, J. G.A. Hatcher and T. Anderson, 1994: Hydrographic data collected in Monterey Bay during 1 September 1988 to 16 December 1992. Monterey Bay Aquarium Research Institute Tech. Rept. 94-15, 549 pp.

Sandstrom, H., 1976: On topographic coupling and generation of internal waves. *Geophys. Fluid Dyn.*, **7,** 231-270.

Shea, R. E. and W. W. Broenkow, 1982: The role of internal tides in the nutrient enrichment of Monterey Bay, California. *Estuarine, Coastal, and Shelf Sci.*, **15,** 57-66.

Shulman, I. and J. K. Lewis, 1995: Optimized boundary conditions for coastal modeling. *Proc. ASCE 4th International Estuarine and Coastal Modeling Conference*, Sponsored by the Waterway, Ports, Coastal, Ocean and Hydraulics Divisions, 268-282.

Slinn, D. N. and J. J. Riley, 1996: Turbulent mixing in the oceanic boundary layer caused by internal wave reflection from sloping terrain. *Dyn. Atmos. Oceans*, **24,** 51-62.

Winant, C. D. and A. W. Bratkovich, 1981: Temperature and currents on the southern California shelf: a description of the variability. *Journal Physical Oceanography*, **11,** 71-86.

Wunsch, C. H., 1968: On the propagation of internal waves up a slope. *Deep-Sea Res.*, **15,** 251-258.

Wunsch, C. H., 1969: Progressive internal waves on slopes. *J. Fluid Mech.*, **35,** 131-144.

Xing, J. and A. M. Davies, 1996: Processes influencing the internal tide, its higher harmonics, and tidally induced mixing on the Malin-Hebrides Shelf. *Progress in Oceanography*, **38,** 155-204.

**Figure 1**. Monterey Bay bathymetry and a sample model bathymetry that incorporates a relatively narrow shelf, a steep (7°) continental slope, a deep basin, and a canyon head lying close to shore.

**Figure 2**. Along-canyon (upper) and cross-canyon (lower left) sections through the model domain showing the vertical distribution of the 30 sigma levels, and a cross-shelf section (lower right) depicting the upper 15 sigma levels.

**Figure 3**. Temperature and salinity profiles used for model initialization, and the corresponding density ($\sigma_\theta$) and buoyancy frequency ($N$) profiles.

**Figure 4**. Cross-shelf sections of $u$ during rising sea level for a sharp (upper) and cosine-shaped (lower) continental shelf break together with characteristics (solid lines) from the linear internal wave dispersion relation including rotation effects.

**Figure 5**. Cross-shelf sections of $u$ at four times during the semidiurnal tidal cycle, as indicated by the stage of the sea level, together with characteristics emanating from the shelf break (solid lines) and reflecting from the coastal boundary (dashed lines). Note the 180° phase shift in horizontal velocity after reflection from the vertical boundary.

**Figure 6**. Case 1 model bathymetry. In plan view, depth is contoured every 200 m from 100 m to 2300 m. The horizontal dotted line indicates the location of the along-canyon ($x$-$z$) slice used for data analyses. The three vertical dotted lines indicate the positions of cross-canyon ($y$-$z$) slices 26, 14, and 2 km from shore.

**Figure 7**. Along-canyon sections of $u$ at four times during the semidiurnal tidal cycle, as indicated by the stage of the sea level, together with characteristics emanating from the shelf break (solid

lines). Note that the velocity scale in Figure 7 has been expanded to ±6 cm $s^{-1}$, versus the ±2 cm $s^{-1}$ scale used for the shelf currents in Figure 5.

**Figure 8**. Along-canyon section of the model *u* (cm $s^{-1}$) at time of high tide (lower), and the observed *u* (cm $s^{-1}$) 2.5 h after M2 high tide (upper), as derived from harmonic analysis of in-situ data (PRP98).

**Figure 9**. Density sections along the critically sloping portion of the model canyon at six times during the tidal cycle. In-situ densities ranging from 1027.35 to 1027.95 kg $m^{-3}$ are contoured at intervals of 0.05 kg $m^{-3}$.

**Figure 10**. Tidal ellipses for the shallowest (left) and deepest (right) model currents, assuming all of the variance is at the M2 frequency. Depths are contoured in 50 m intervals starting at 100 m.

**Figure 11**. Along-canyon sections of M2 *u* amplitude (upper) and energy density, E, (lower) with characteristics emanating from the shelf break (solid lines) and reflecting from the coastal boundary (dashed lines).

**Figure 12**. Case 1 cross-canyon sections of energy density, E. Note that a different vertical scale is used for each section.

**Figure 13**. Total energy in three cross-canyon sections (positions indicated in Figure 6) for model case 2 (Figure 18). Total energy values are shown for two additional cross-canyon sections for case 1 (Figure 12). Each value represents energy integrated over a volume 31 km alongshore by 1 km cross-shore by depth.

**Figure 14**. Cross-canyon density sections 2 km from the eastern boundary at six times during the tidal cycle. The in-situ densities are contoured in intervals of 0.03 kg $m^{-3}$, and range from 26.335 kg $m^{-3}$ to 26.635 kg $m^{-3}$.

**Figure 15**. Along-shelf section of *v* 2 km from model eastern boundary showing evolution of the internal tide from beam-like near the canyon rims to first mode-like further away.

**Figure 16**. Bathymetry for model cases 1 and 2, as described in Table 1, are shown. The contour interval is 100 m.

**Figure 17**. Case 2 energy density, E (J $m^{-3}$), along-canyon sections. The canyon floor slope for each case is indicated. The canyon is 11 km wide at the rim and 3 km wide at the floor in all three studies. Bottom profiles for the continental shelf and slope adjacent to the canyon (dashed lines) are also shown.

**Figure 18**. Case 2 energy density, E (J $m^{-3}$), cross-canyon sections 26 km (upper), 14 km (middle), and 2 km (lower) from the eastern boundary.

TABLE 1. Canyon slopes and widths for the numerical simulation cases discussed in the text.

| **Case Number** | **Continental Slope Shape** | **Canyon Floor Slope (°)** | **Canyon Rim Width (km)** | **Canyon Floor Width (km)** |
|---|---|---|---|---|
| 0a | linear | | | |
| 0b | cosine | | | |
| 1 (Montere y Canyon) | cosine | 1.55 | 11 → 3 | 3 |
| 2a | cosine | 0.74 | 11 | 3 |
| 2b | cosine | 1.55 | 11 | 3 |
| 2c | cosine | 2.29 | 11 | 3 |

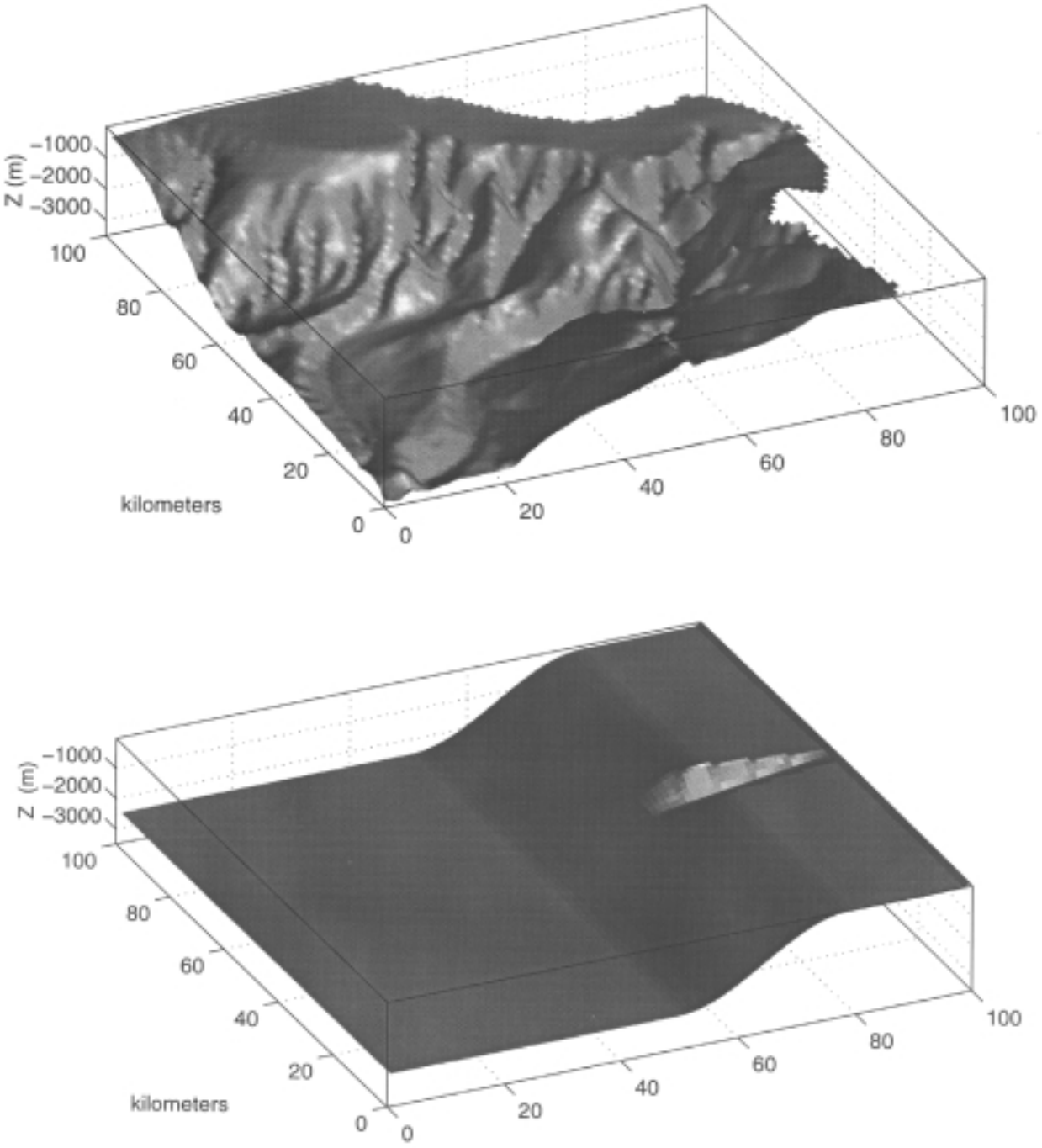


**Figure 1**. Monterey Bay bathymetry and a sample model bathymetry that incorporates a relatively narrow shelf, a steep (7°) continental slope, a deep basin, and a canyon head lying close to shore.

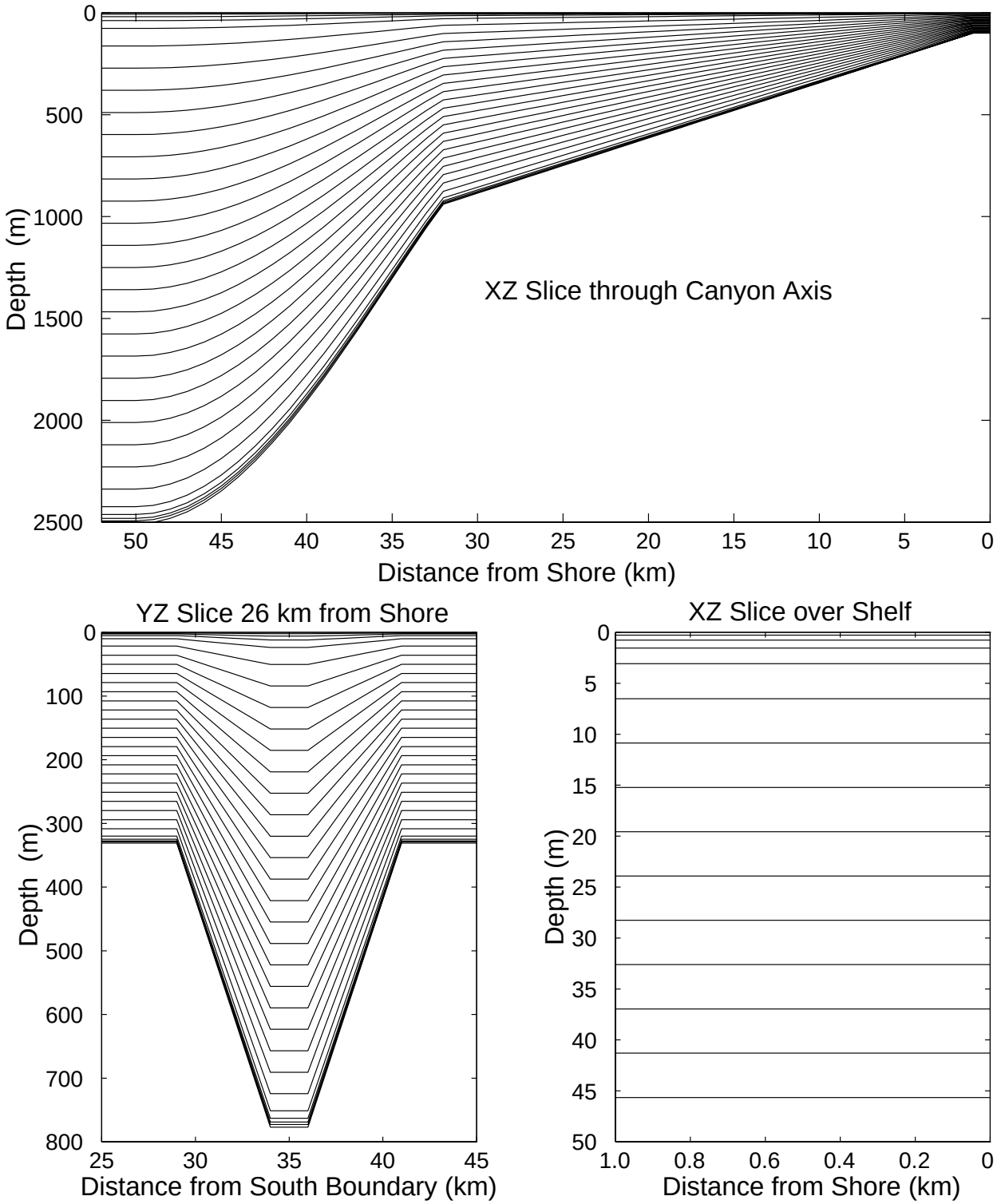


**Figure 2**. Along-canyon (upper) and cross-canyon (lower left) sections through the model domain showing the vertical distribution of the 30 sigma levels, and a cross-shelf section (lower right) depicting the upper 15 sigma levels.

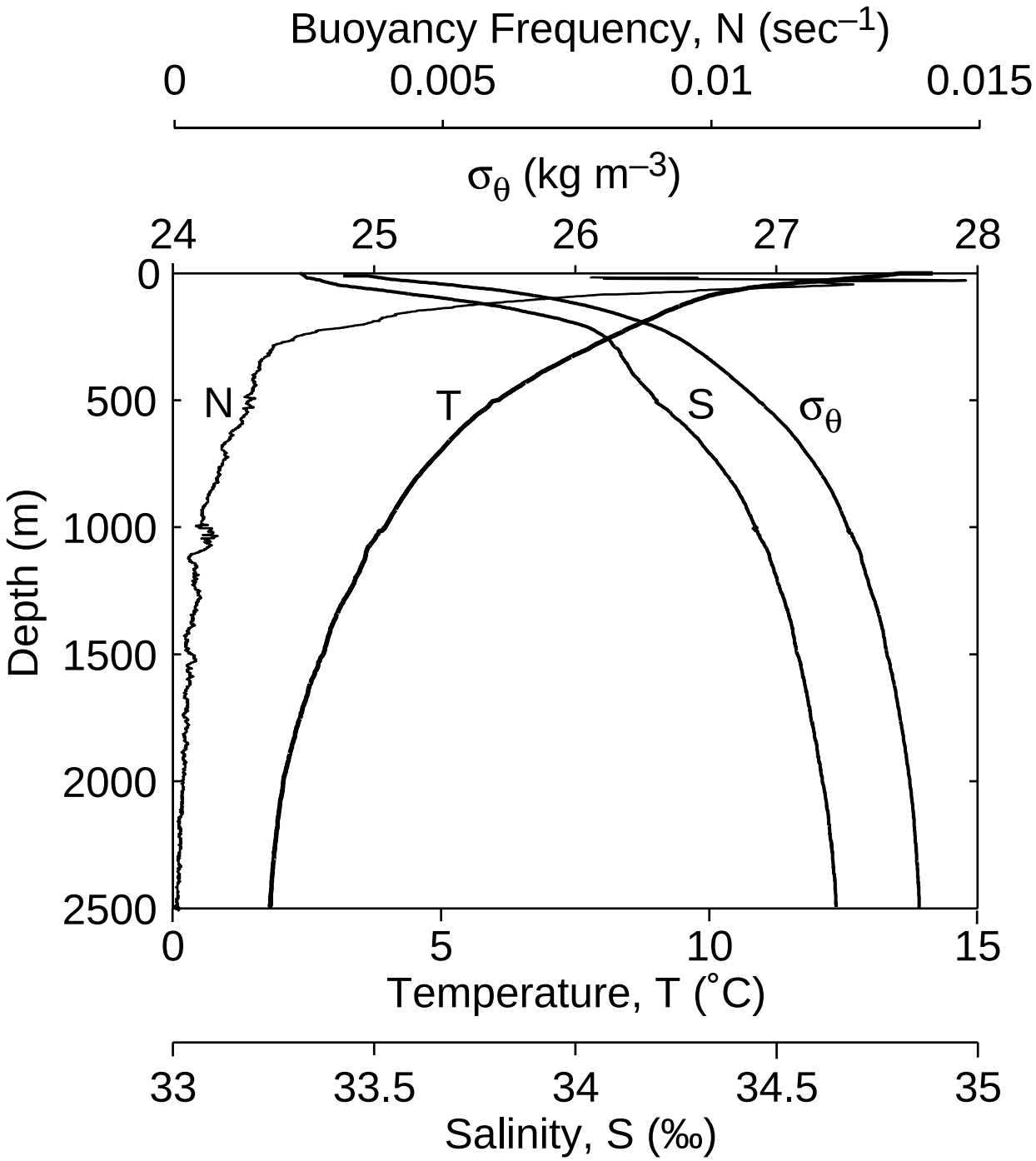


**Figure 3**. Temperature and salinity profiles used for model initialization, and the corresponding density ($\sigma_\theta$) and buoyancy frequency ($N$) profiles.

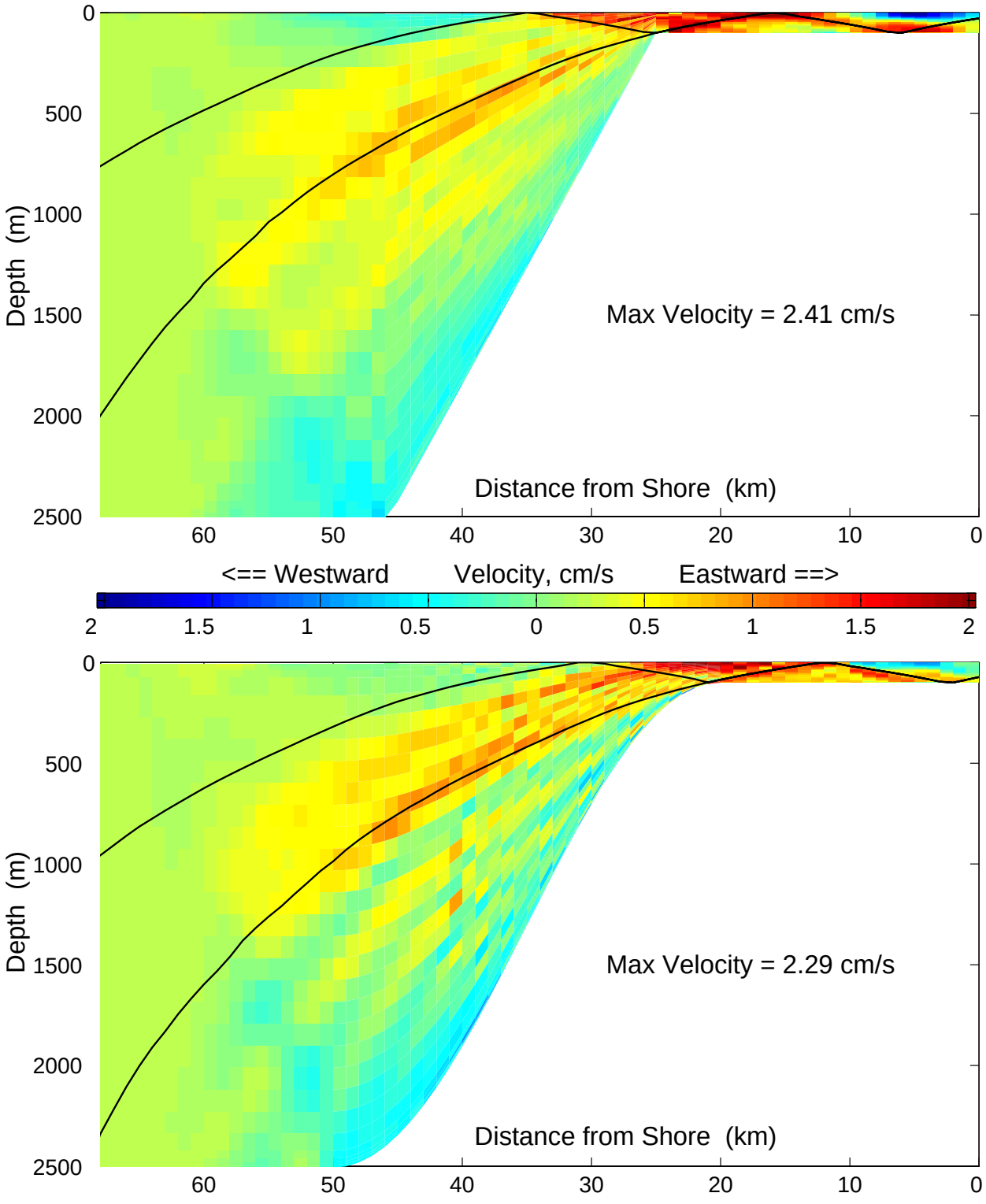


**Figure 4**. Cross-shelf sections of $u$ during rising sea level for a sharp (upper) and cosine-shaped (lower) continental shelf break together with characteristics (solid lines) from the linear internal wave dispersion relation including rotation effects.

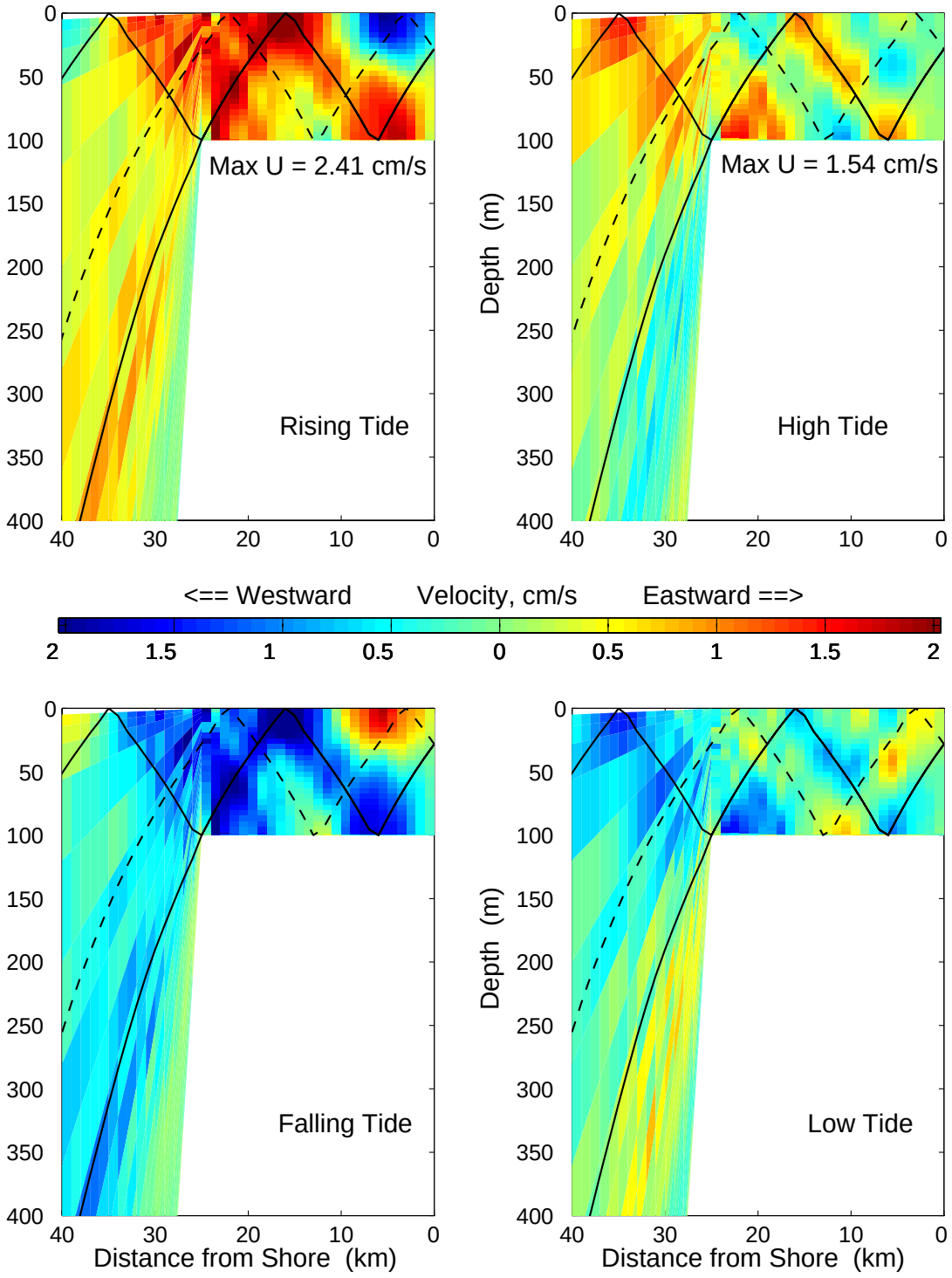


**Figure 5**. Cross-shelf sections of $u$ at four times during the semidiurnal tidal cycle, as indicated by the stage of the sea level, together with characteristics emanating from the shelf break (solid lines) and reflecting from the coastal boundary (dashed lines). Note the 180° phase shift in horizontal velocity after reflection from the vertical boundary.

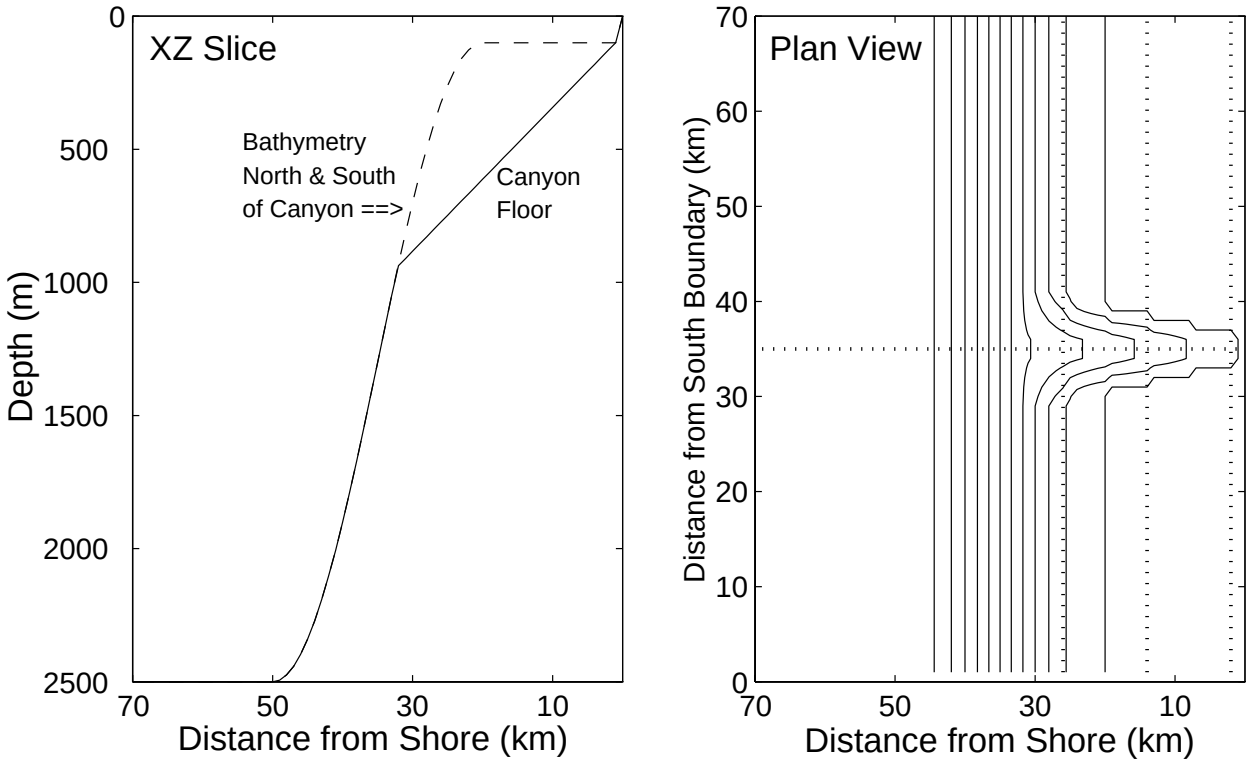


**Figure 6**. Case 1 model bathymetry. In plan view, depth is contoured every 200 m from 100 m to 2300 m. The horizontal dotted line indicates the location of the along-canyon ($x$-$z$) slice used for data analyses. The three vertical dotted lines indicate the positions of cross-canyon ($y$-$z$) slices 26, 14, and 2 km from shore.

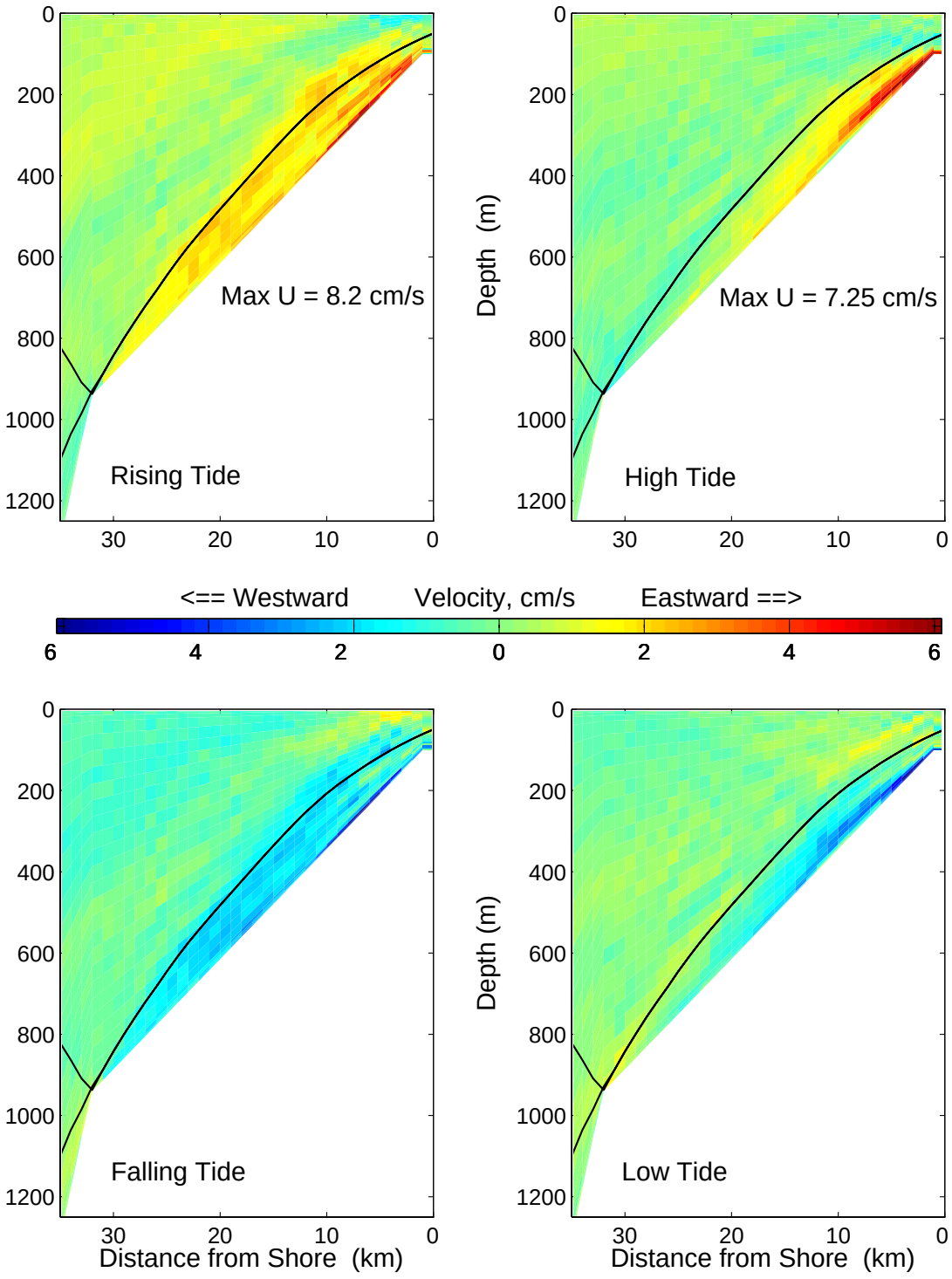


**Figure 7**. Along-canyon sections of $u$ at four times during the semidiurnal tidal cycle, as indicated by the stage of the sea level, together with characteristics emanating from the shelf break (solid lines). Note that the velocity scale in Figure 7 has been expanded to ±6 cm $s^{-1}$, versus the ±2 cm $s^{-1}$ scale used for the shelf currents in Figure 5.

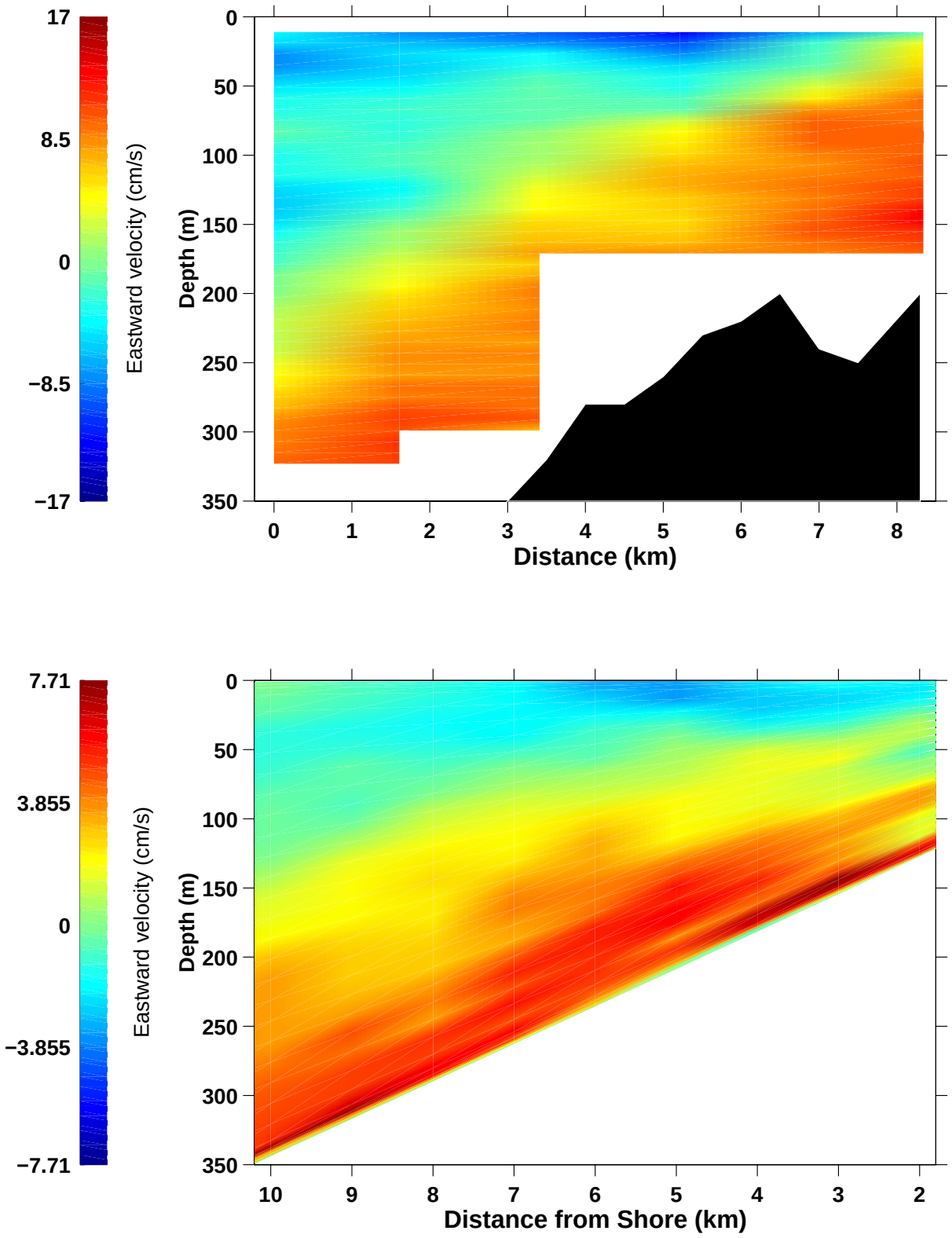


**Figure 8**. Along-canyon section of the model $u$ (cm $s^{-1}$) at time of high tide (lower), and the observed $u$ (cm $s^{-1}$) 2.5 h after M2 high tide (upper), as derived from harmonic analysis of in-situ data (PRP98).

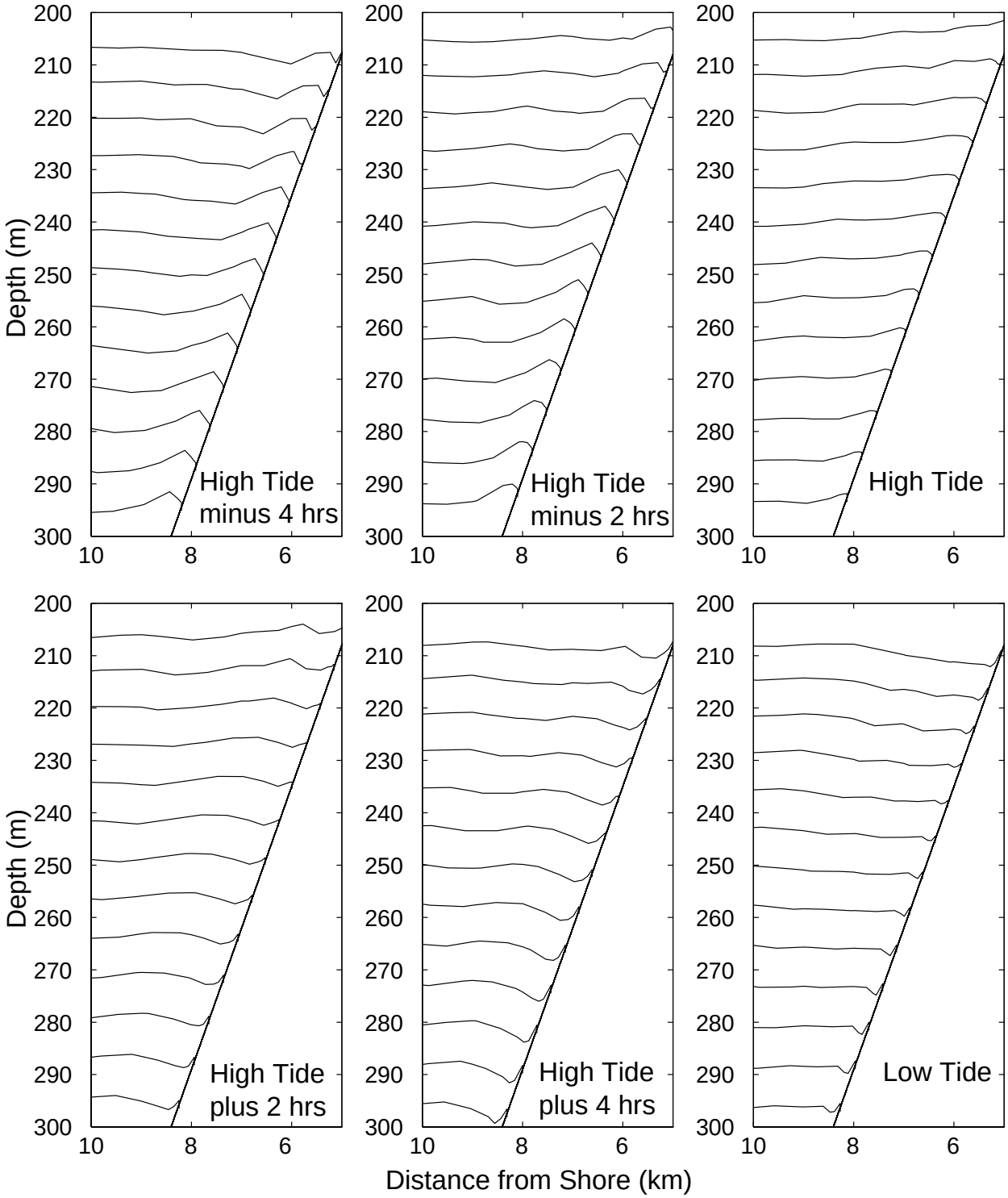


**Figure 9**. Density sections along the critically sloping portion of the model canyon at six times during the tidal cycle. In-situ densities ranging from 1027.35 to 1027.95 kg $m^{-3}$ are contoured at intervals of 0.05 kg $m^{-3}$.

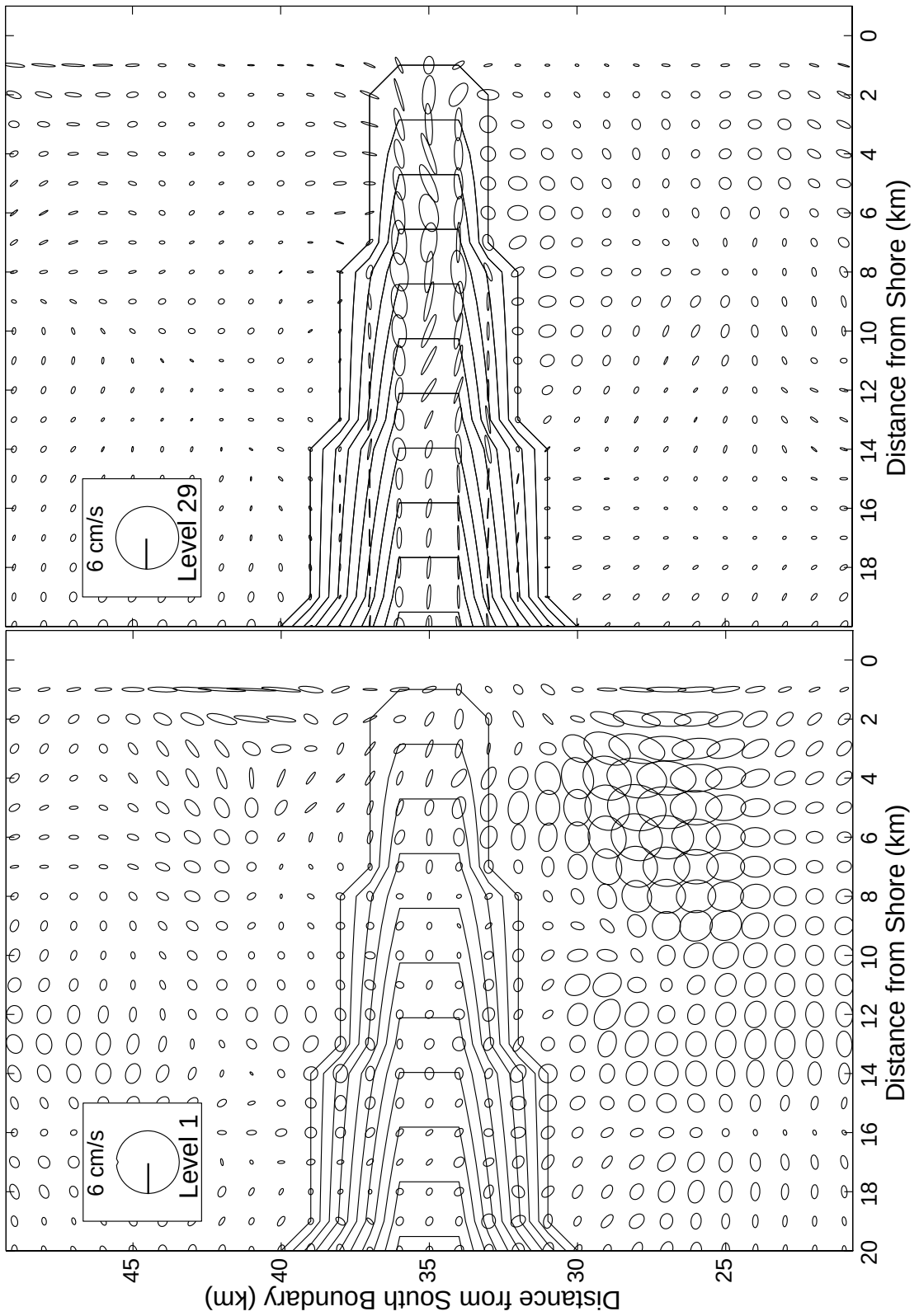


**Figure 10**. Tidal ellipses for the shallowest (left) and deepest (right) model currents, assuming all of the variance is at the M2 frequency. Depths are contoured in 50 m intervals starting at 100 m.

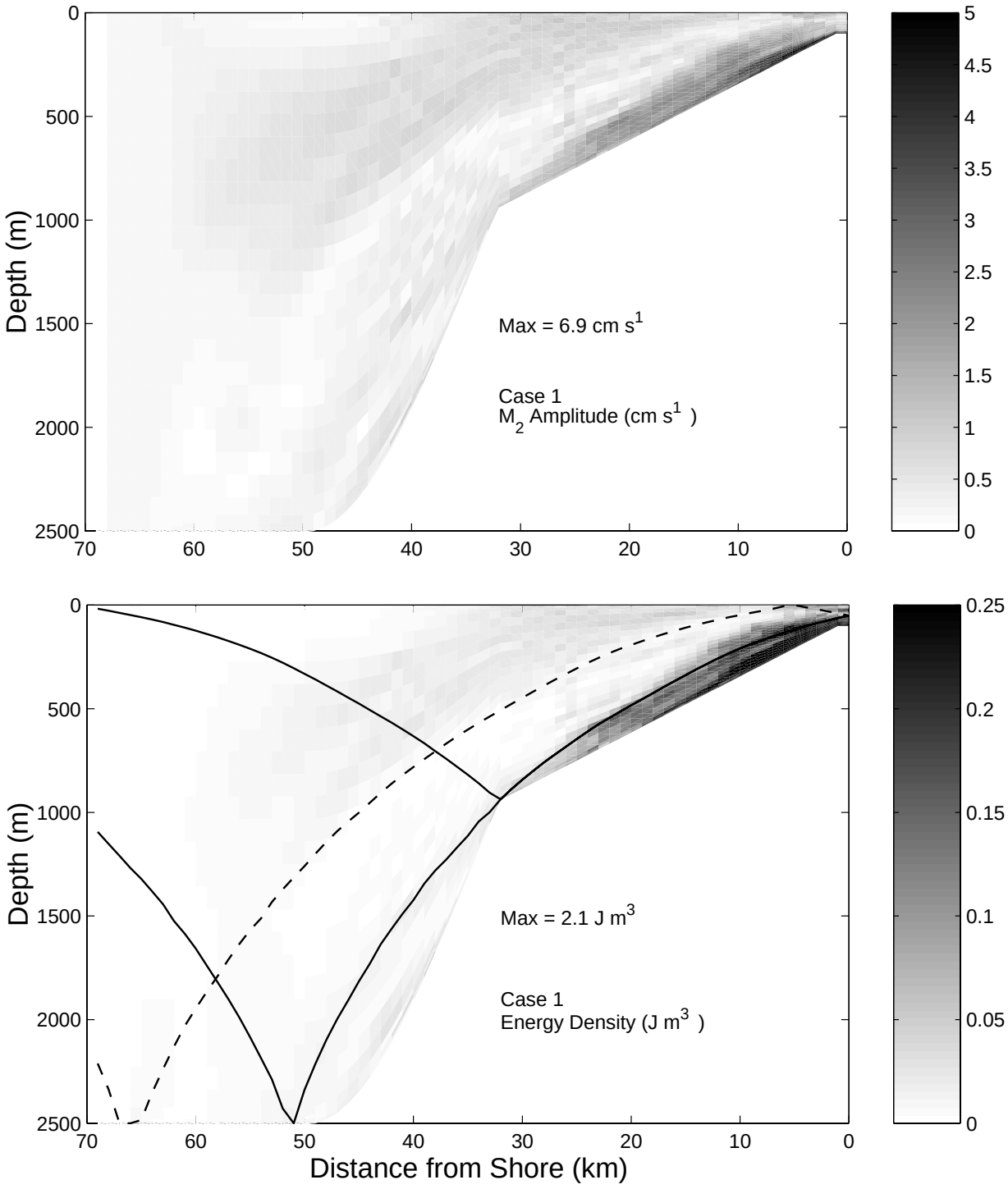


**Figure 11**. Along-canyon sections of M2 *u* amplitude (upper) and energy density, E, (lower) with characteristics emanating from the shelf break (solid lines) and reflecting from the coastal boundary (dashed lines).

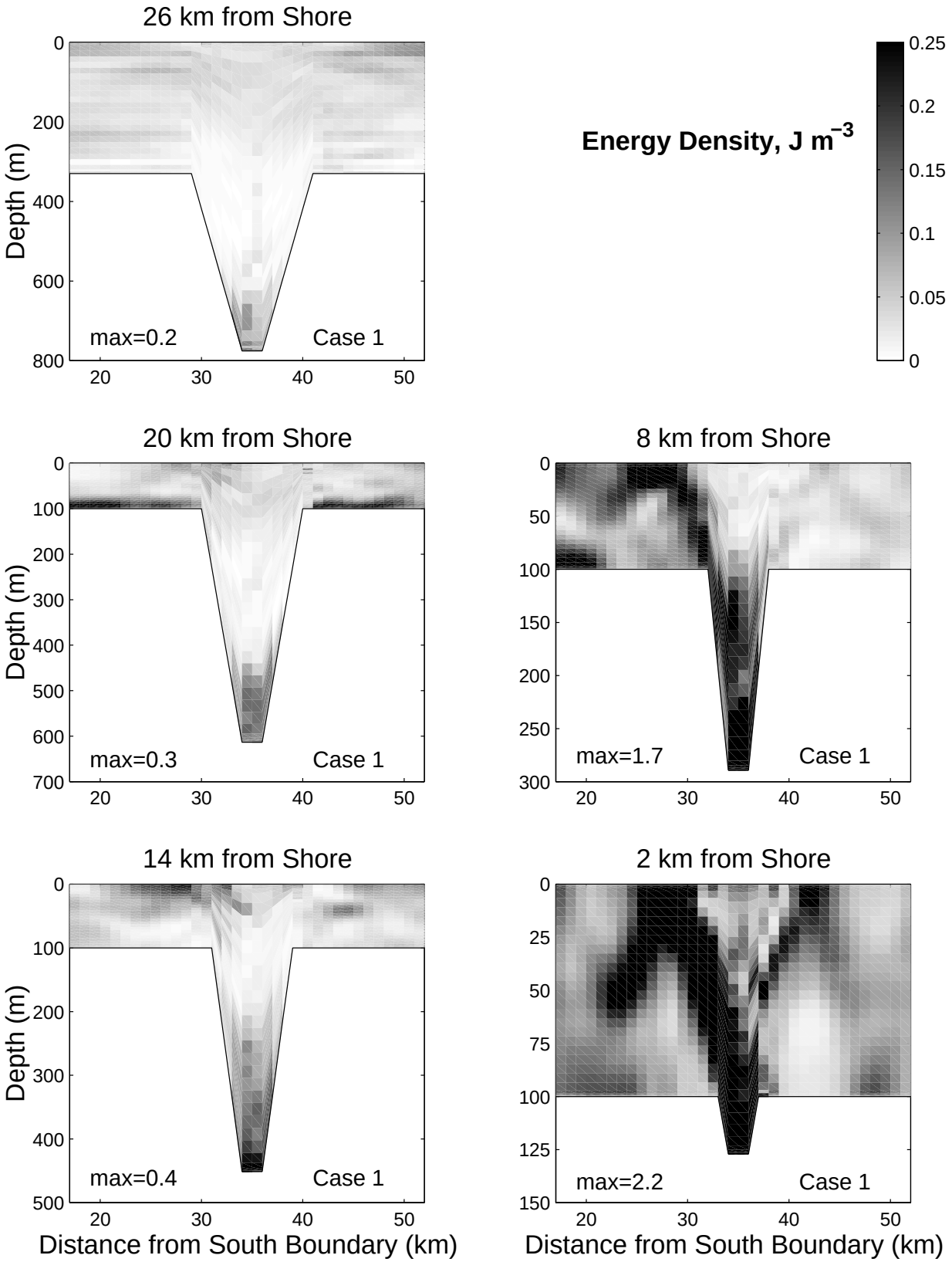


**Figure 12**. Case 1 cross-canyon sections of energy density, E. Note that a different vertical scale is used for each section.

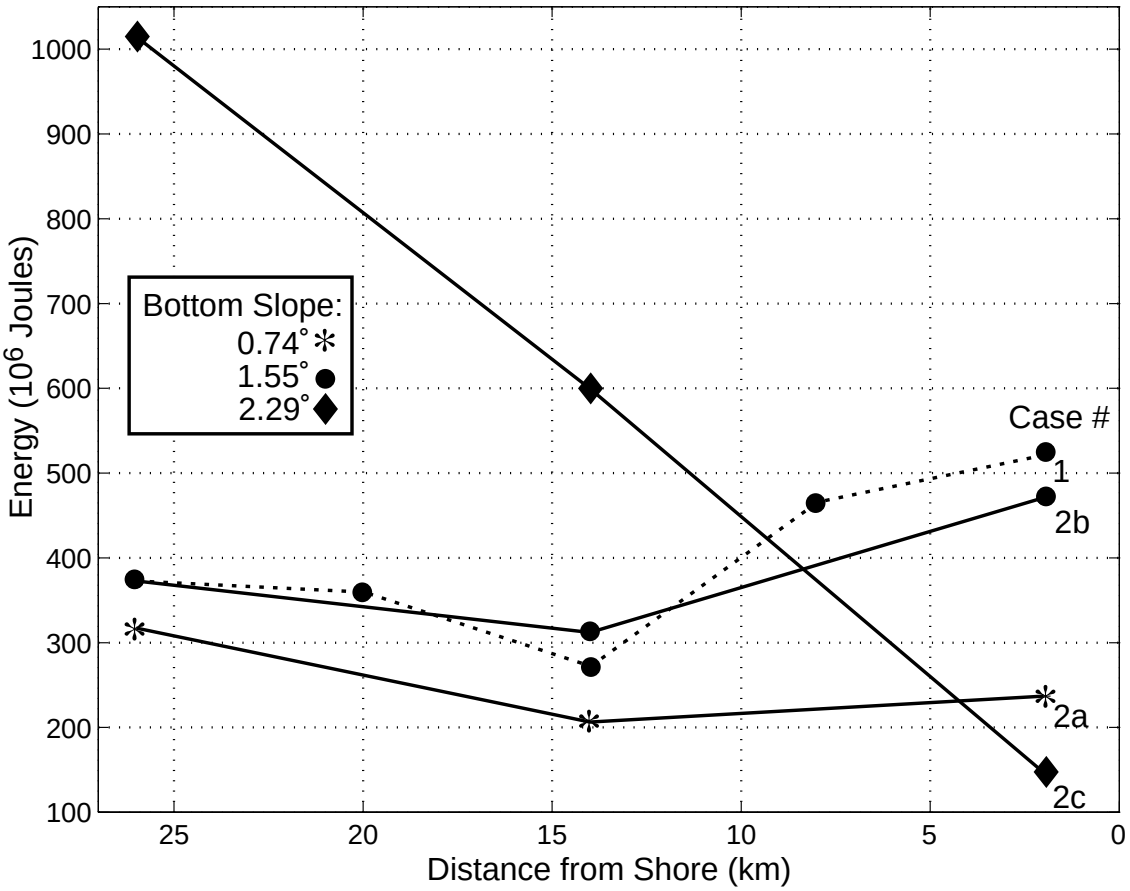


**Figure 13**. Total energy in three cross-canyon sections (positions indicated in Figure 6) for model case 2 (Figure 18). Total energy values are shown for two additional cross-canyon sections for case 1 (Figure 12). Each value represents energy integrated over a volume 31 km alongshore by 1 km cross-shore by depth.

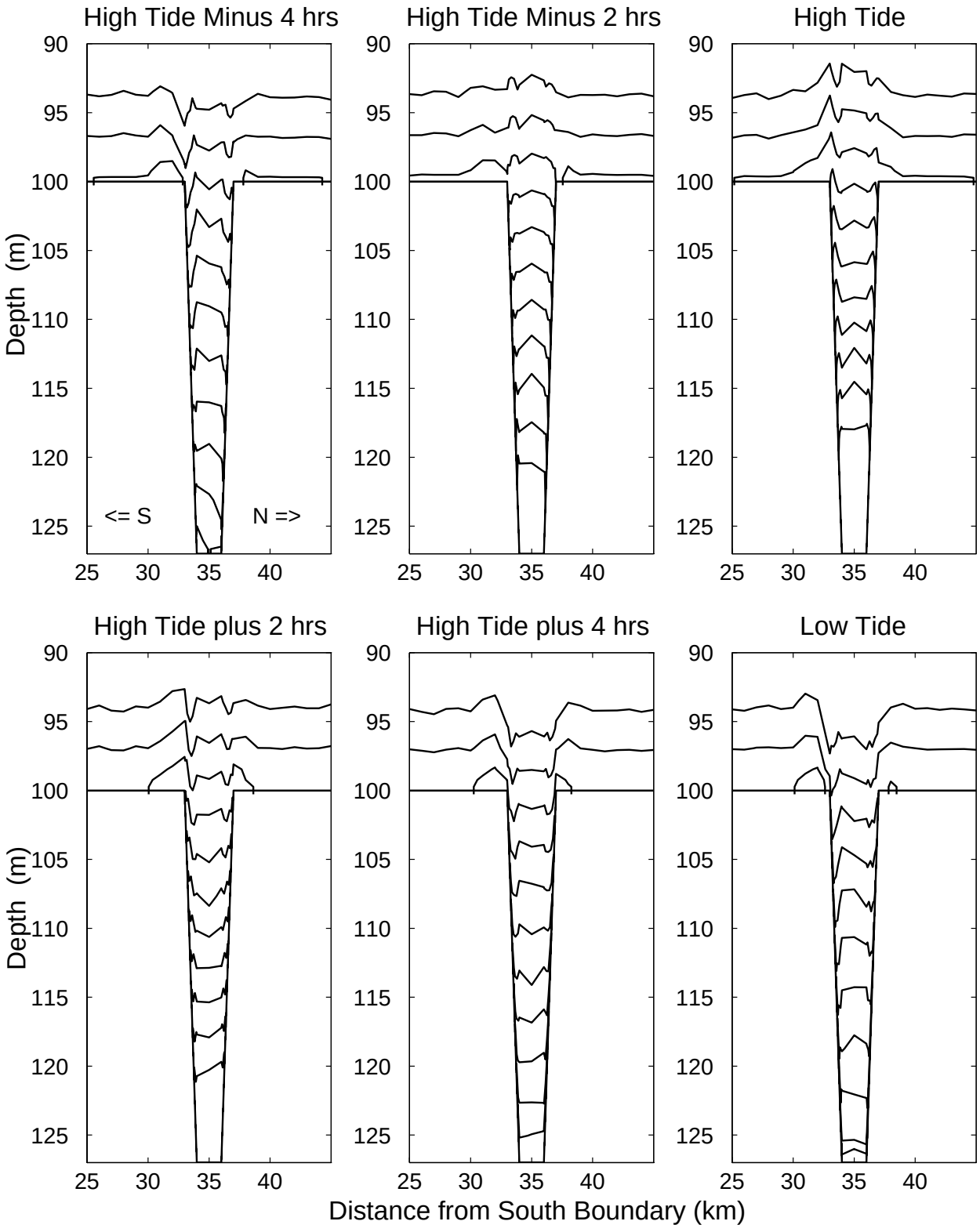


**Figure 14**. Cross-canyon density sections 2 km from the eastern boundary at six times during the tidal cycle. The in-situ densities are contoured in intervals of 0.03 kg $m^{-3}$, and range from 26.335 kg $m^{-3}$ to 26.635 kg $m^{-3}$.

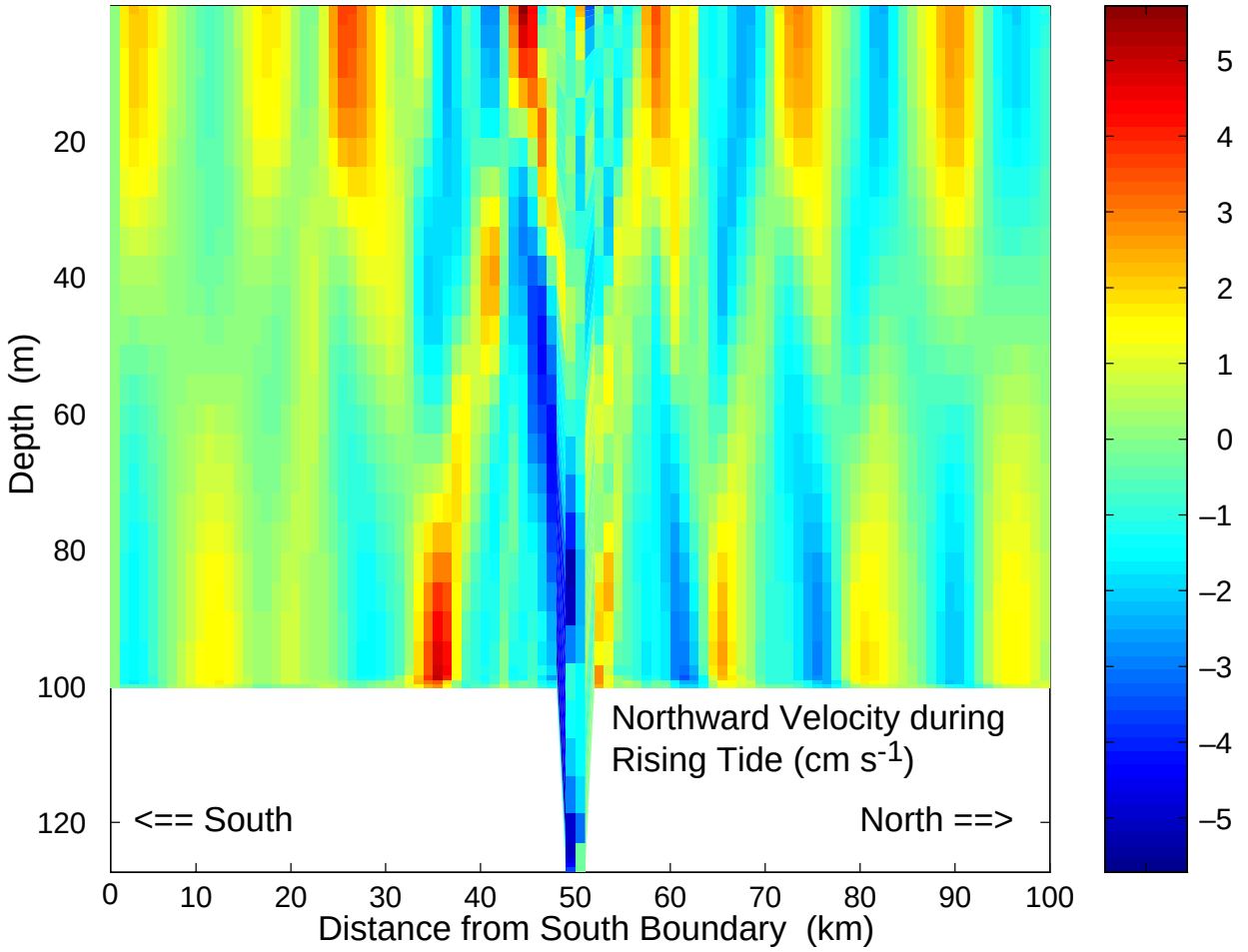


**Figure 15**. Along-shelf section of $v$ 2 km from model eastern boundary showing evolution of the internal tide from beam-like near the canyon rims to first mode-like further away.

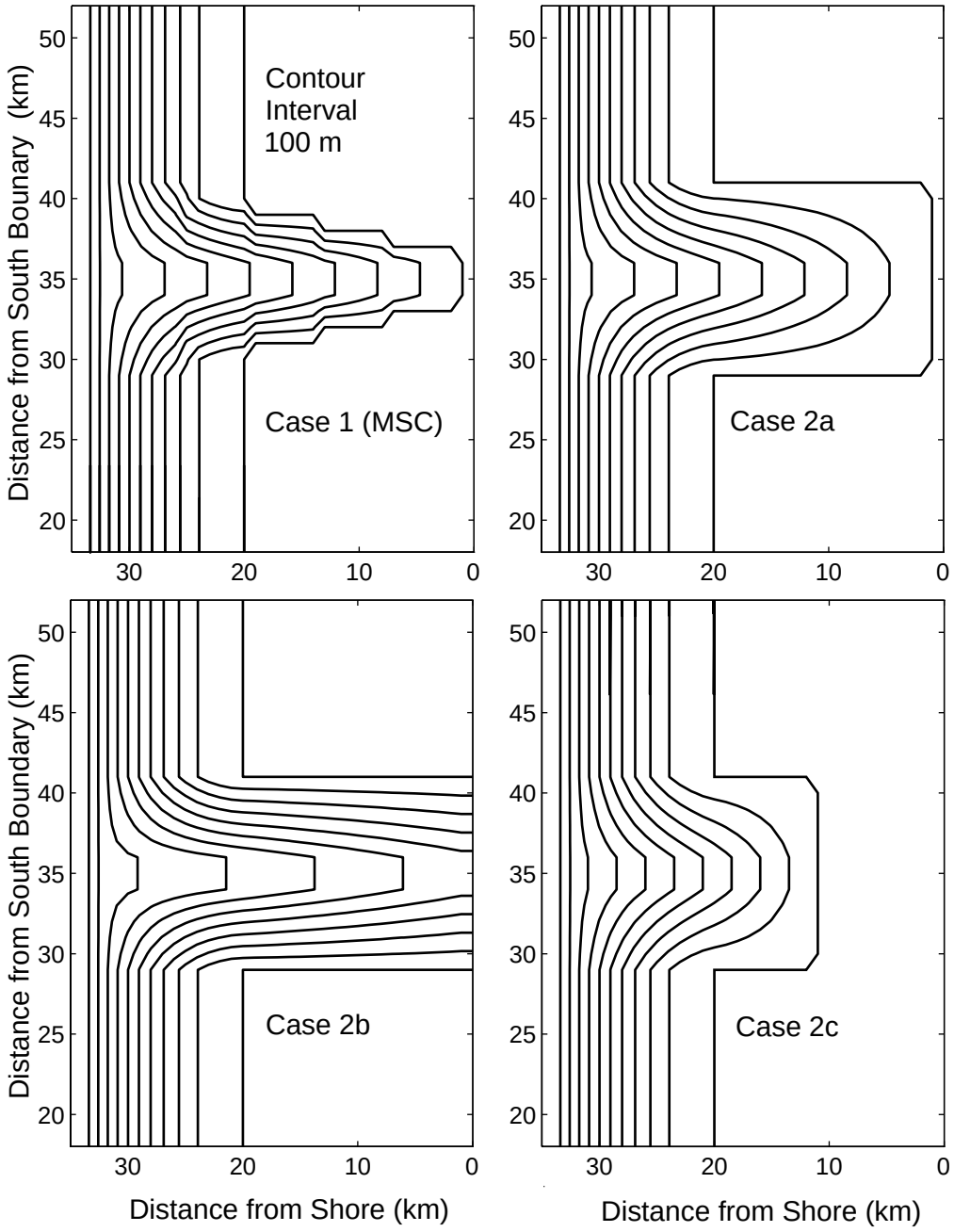


**Figure 16**. Bathymetry for model cases 1 and 2, as described in Table 1, are shown. The contour interval is 100 m.

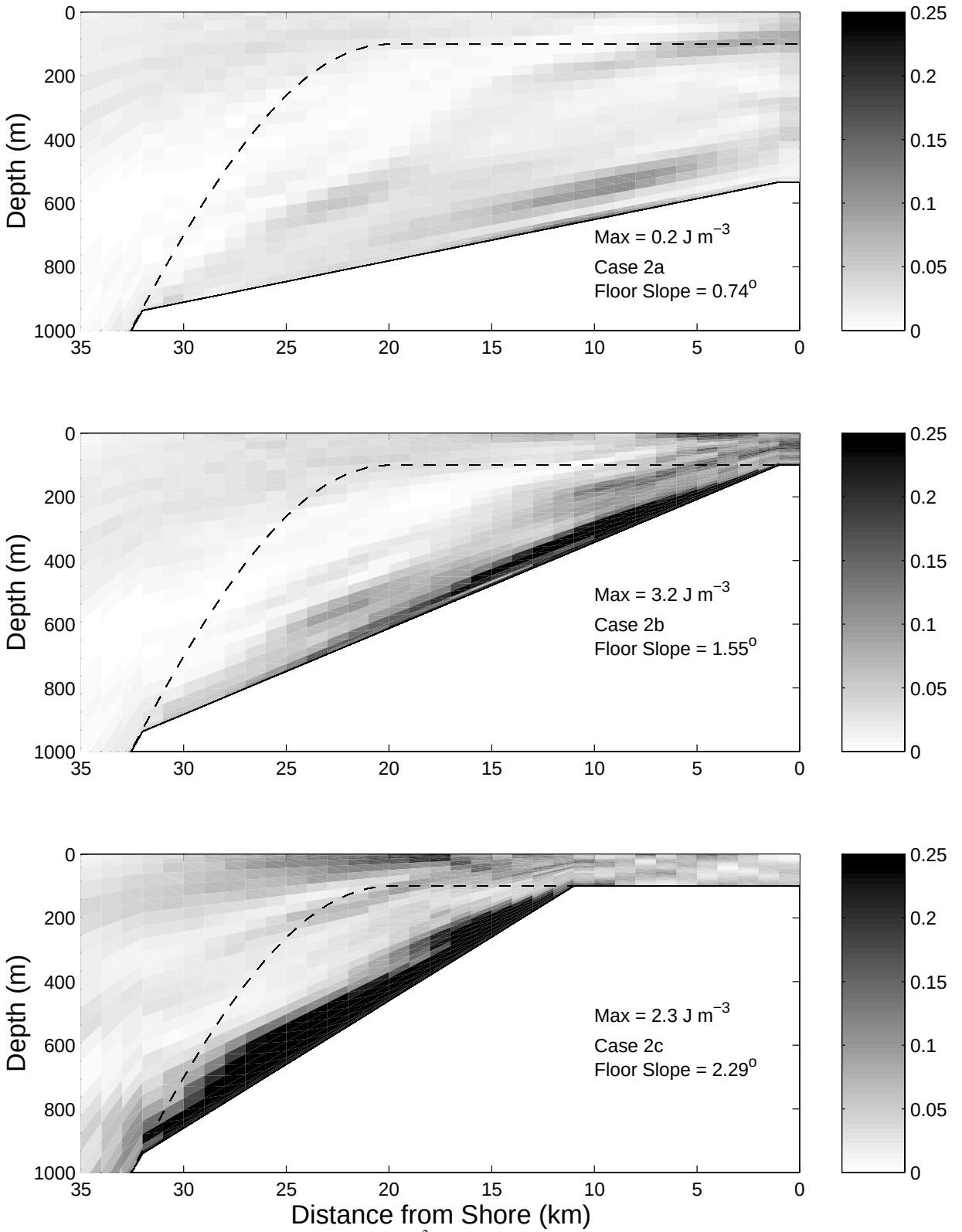


**Figure 17**. Case 2 energy density, E (J $m^{-3}$), along-canyon sections. The canyon floor slope for each case is indicated. The canyon is 11 km wide at the rim and 3 km wide at the floor in all three studies. Bottom profiles for the continental shelf and slope adjacent to the canyon (dashed lines) are also shown.

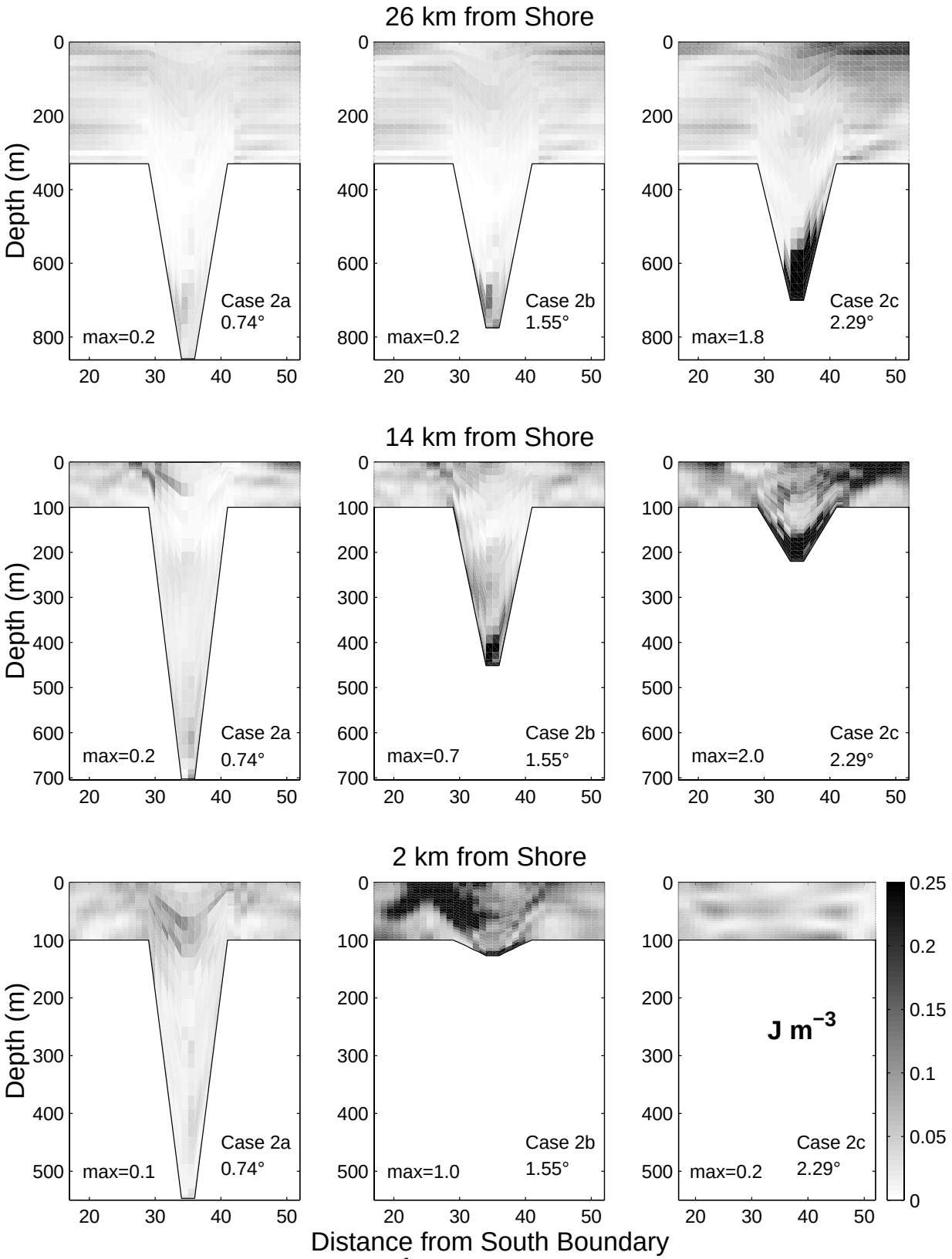


**Figure 18**. Case 2 energy density, E (J $m^{-3}$), cross-canyon sections 26 km (upper), 14 km (middle), and 2 km (lower) from the eastern boundary.